Superfluid ^{3}He Josephson weak links

J. C. Davis and R. E. Packard

Department of Physics, University of California, Berkeley, California 94720

(Published 19 July 2002)

Josephson weak links between samples of macroscopic quantum systems such as superconductors, superfluids, and Bose-Einstein condensates provide a unique tool with which to explore quantum mechanics and an opportunity to create applications based on macroscopic quantum physics. In this review we describe the development of the field of weak links in superfluid ^{3}He. We review the basic techniques used to study this system and then describe the experimental and theoretical milestones that have led to our present understanding.

CONTENTS

I. INTRODUCTION

Superfluids, like superconductors and Bose-Einstein condensates (BEC's), are examples of systems in which a finite fraction of all the constituent particles resides in the same quantum state. When two samples of such a system are "weakly coupled" together, a variety of interesting physical effects occur due to the existence of a well-defined quantum phase ϕ (London, 1945; Feynman, 1955; Anderson, 1964; Tilley and Tilley, 1990), which is a macroscopic coordinate in the material. During the past four decades superconducting Josephson devices (tunnel junctions and microbridges) have been the prototypical elements for the demonstration of a wide diversity of physical phenomena, and some of the effects have led to significant practical applications [e.g., superconducting quantum interference device (SQUID) magnetometers and voltage standards].

This article reviews recent progress in the physics of Josephson weak links coupling samples of superfluid ^{3}He. We begin by giving a heuristic derivation of the celebrated Josephson equations (Josephson, 1962) for the general case of two weakly coupled macroscopic quantum systems. We then remind the reader of some of the most striking phenomena that exist in weakly coupled superconductors: Josephson oscillations, the Shapiro effect, plasma oscillations, and quantum interference as exemplified by the dc SQUID. After discussing the role of healing length in determining the strength of the coupling, we describe some of the key experimental techniques for probing the properties of superfluid ^{3}He weak links. The main body of this review covers the key experimental and theoretical developments related to the remarkable manifestations of weak-coupling physics in superfluid ^{3}He.

II. JOSEPHSON EQUATIONS À LA FEYNMAN

The governing equations for two weakly coupled macroscopic quantum systems can be derived from several different viewpoints. For simplicity we follow the heuristic derivation of Feynman (Feynman *et al.*, 1963). Although originally intended to describe superconducting phenomena, this approach is quite general for the weak coupling of any two macroscopic systems.

We consider a particle that could be in either of two samples of superfluid (labeled samples 1 and 2) which are brought into some kind of weak coupling with each other as shown schematically in Fig. 1(a). The represen-

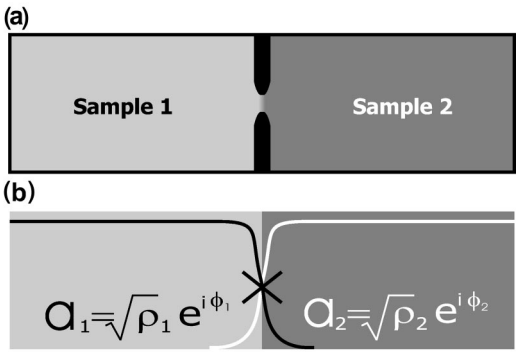

FIG. 1. Weak coupling between two superfluid samples: (a) a schematic arrangement of two containers of superfluid separated by a small aperture; (b) a schematic view of the overlap of two unperturbed functions, u_1 and u_2, showing their independent magnitudes as a function of position at the weak link.

tative particle is under the influence of a Hamiltonian $H=H_0+H_1$, where H_0 describes an uncoupled system and H_1 the coupling through the weak link.

In the presence of a weak-coupling term, the total wave function Ψ can be written as a superposition of the uncoupled states u_1 and u_2, which represent the eigenstates for finding the particle on side 1 or 2, where the energies are E_1 or E_2, respectively. Thus

$$H_0 u_{1,2} = E_{1,2} u_{1,2} \tag{1}$$

and

$$i\hbar \frac{\partial \Psi}{\partial t} = H\Psi = (H_0 + H_1)\Psi. \tag{2}$$

We let $\Psi = a_1 u_1 + a_2 u_2$ and take the inner product of the Schrödinger equation with u_1. This gives

$$\begin{aligned} i\hbar \frac{\partial a_1}{\partial t} &= E_1 a_1 + a_1 \langle u_1 | H_1 u_1 \rangle + H_{12} a_2 \\ &= a_1 E_1' + H_{12} a_2, \end{aligned} \tag{3}$$

where H_{12} is the matrix element $\langle u_1 | H_1 u_2 \rangle$.

Similarly, if we take the scalar product of the Schrödinger equation with u_2, we get

$$\begin{aligned} i\hbar \frac{\partial a_2}{\partial t} &= E_2 a_2 + a_2 \langle u_2 | H_1 u_2 \rangle + H_{21} a_1 \\ &= a_2 E_2' + H_{12} a_1, \end{aligned} \tag{4}$$

where we have used the fact that, for a real perturbation, $H_{12}=H_{21}$.

The amplitudes a_1 and a_2 are complex numbers, which can be written as $a_1=\sqrt{\rho_1}e^{i\phi_1}$ and $a_2=\sqrt{\rho_2}e^{i\phi_2}$, where the symbols ρ_1 and ρ_2 represent the mass density of particles within the "condensed" fraction of the system. Substitution of these amplitudes into Eq. (1) yields two equations from the real and imaginary components. One equation reveals that the mass current $I \equiv \dot{\rho}_1$ is given by

$$I = \frac{2H_{12}}{\hbar} \sqrt{\rho_1 \rho_2} \sin(\phi_2 - \phi_1) \equiv I_c \sin\phi, \tag{5}$$

where the second equality defines both the critical current I_c and the phase difference $\phi \equiv \phi_2 - \phi_1$. One finds from the other equation that

$$\phi(t) = \phi_0 - \frac{1}{\hbar} \int (E_2' - E_1') dt, \tag{6}$$

where the energy E_i' equals $E_i + \langle u_i | H_1 | u_i \rangle$.

For a macroscopic quantum system the energy difference $E_2' - E_1'$ is equal to the chemical-potential difference $\Delta\mu$ between the two sides, so we may write

$$\phi(t) = \phi_0 - \frac{1}{\hbar} \int \Delta\mu\, dt \tag{7}$$

or, equivalently,

$$\frac{d\phi}{dt} = -\frac{\Delta\mu}{\hbar}. \tag{8}$$

Although the derivation was carried out in the context of two weakly coupled systems, the phase evolution equation is much more general (Packard, 1998) and describes the phase evolution between any two points in a macroscopic quantum system (e.g., superfluid ^{4}He, superfluid ^{3}He-B, superconductors, and Bose-Einstein condensates) whether weakly coupled or not. Since the chemical-potential difference is the energy difference between particles at two positions, Eq. (8) is equivalent to saying that there exists a macroscopic wave function that describes the system and that function has a time-dependent phase varying as $e^{-iEt/\hbar}$ (as in the single-particle case). Equations (7) and (8) simply state that if an energy difference exists between two points, the phase difference changes with time in a fashion familiar from microscopic quantum physics.

Equations (5) and (8) were first discovered by Josephson (1962) in the context of Cooper-pair tunneling through an insulating barrier, so-called "Josephson tunneling." We note that the terms "Josephson equation" and "Josephson effect" have been associated with very many different phenomena occurring in many types of weak links in many different physical situations. For clarity, we shall use these terms sparingly and only as defined in the text. Weak links characterized by the sinelike $I(\phi)$ [Eq. (5)] will be referred to as *Josephson weak links*. Structures having local suppressed superconductivity (or superfluidity) but exhibiting a current-phase relation $I(\phi)$ different from Eq. (5) we shall simply call *weak links*. We also distinguish Josephson weak links from ^{4}He devices in which phase slippage occurs by the passage of vortices.

We shall refer to Eq. (5) as the Josephson current-phase relation and Eqs. (7) or (8) as the Josephson-Anderson phase evolution equation. Note that Eq. (8) is often called the ac Josephson equation or the Josephson frequency relation. However, since this equation describes the general evolution of the phase difference (not necessarily a periodic phenomenon), we shall refrain from this misnomer.

III. SUPERCONDUCTING WEAK LINKS

After Josephson's pioneering paper (1962), experiments on superconducting tunnel junctions soon showed

that Josephson's tunneling currents existed, and many beautiful effects connected with Eqs. (5) and (8) were subsequently discovered (Van Duzer and Turner, 1981; Barone and Paternò, 1982; Likharev, 1986). Since the only requirement for the validity of Eqs. (5) and (8) is weak coupling between two macroscopic quantum samples, it is not surprising that other weakly coupled superconducting systems were soon also found to follow these equations. In particular, constricting a superconductor into a narrow "bridge" between two macroscopic samples will produce a device with a $\sin\phi$ current-phase relation (Dayem and Grimes, 1966). Quantum tunneling is not required. The criterion for the bridge weak-link geometry is that the length and at least one transverse dimension of the link should be on the order of the superconducting healing length ξ (the characteristic minimum length for wave-function variations near a boundary). For example, in aluminum $\xi \sim 150$ nm and photolithography techniques can readily produce Dayem bridges that obey Eqs. (5) and (8).

There is a vast literature describing many fascinating effects associated with superconducting systems weakly coupled in this fashion (Van Duzer and Turner, 1981; Barone and Paternò, 1982; Likharev, 1986; Tilley and Tilley, 1990). Here we shall mention only a few phenomena that have played a pivotal role in the science of superconducting weak links.

A. Josephson oscillations

If a fixed electric-potential difference V is established between two weakly coupled superconductors, the chemical-potential difference between Cooper pairs on the two sides is given by

$$\Delta\mu = 2\ \mathrm{eV}. \tag{9}$$

Using this in Eq. (8) and applying the result to Eq. (5) immediately leads us to the prediction that a constant voltage should produce supercurrents oscillating at the so-called Josephson frequency,

$$\omega_j = \frac{\Delta\mu}{\hbar} = \frac{2\ \mathrm{eV}}{\hbar} = 2\pi \cdot 484\ \ \mathrm{THz/V}. \tag{10}$$

The existence of these currents, which are typically at very high frequencies, is usually inferred from the detection of microwaves radiating from superconducting Josephson weak links (Langenberg *et al.*, 1965) biased with potential differences on the order of 10^{-3} V.

B. Shapiro steps

If the potential difference applied across a superconducting Josephson weak link contains an ac component V_{ac} as well as a dc component, then this ac modulation may mix with the Josephson oscillation to produce a dc current (Josephson, 1962). This occurs when the Josephson frequency associated with the applied dc component, ω_J, is an integral multiple of the frequency of the applied ac voltage ω. As a function of ω, current enhancement steps appear in the dc current-voltage characteristic whenever

$$\omega_j = n\omega, \quad n = 0,1,2,\ldots . \tag{11}$$

For a given n, the magnitude of the current enhancement I_n depends on the nth-order Bessel function whose argument is proportional to the applied ac voltage V_{ac}:

$$I_n = I_c \left| J_n\left(\frac{2\ \mathrm{eV_{ac}}}{\hbar\omega}\right)\right|. \tag{12}$$

This heterodyning effect was predicted in Josephson's original paper and confirmed experimentally soon afterwards (Shapiro, 1963).

A related effect is seen when a dc-voltage-biased Josephson weak link is placed in a microwave resonant cavity. Then the microwave radiation emitted by the oscillating currents in the weak link can excite cavity modes which themselves will mix with the Josephson oscillations and cause a dc current enhancement. Thus when the Josephson frequency satisfies Eq. (11), where ω is now a cavity resonance frequency, a current spike appears in the current-voltage (I-V) curve. This so-called Fiske effect (Barone and Paternò, 1982) can be thought of as a homodyne analog of the Shapiro effect.

C. Plasma mode

A real superconducting Josephson weak link may be described by an electric equivalent circuit that consists of a parallel combination of a capacitor, an ideal weak link (i.e., an element exhibiting a $\sin\phi$ current-phase relation), and a resistor. For currents that are small compared to I_c, the weak-link element acts as a linear inductance L_J with magnitude given by

$$L_J = \frac{\Phi_0}{2\pi I_c}, \tag{13}$$

where $\Phi_0 = h/2e$ is the quantum of magnetic flux. This parallel combination of capacitive and inductive elements has a resonant mode that has been observed (Dahm *et al.*, 1968) and well studied in the microwave region of the spectrum (Likharev, 1986). This mode is often referred to as the plasma mode.

D. Quantum interference

In superconducting Josephson weak links there are several interference effects related to the wave-function phase shifts caused by magnetic fields. Perhaps the most important example is that of the dc SQUID (Jaclevic *et al.*, 1964; Clarke, 1996). This consists of the parallel connection of two $\sin\phi$ junctions or weak links as shown in Fig. 2. The total current through the device is proportional to the sine of the phase difference across it, $I = I_{\max}\sin\phi$. The maximum current $I_{\max}$ is modulated by the magnetic flux Φ through the circuit:

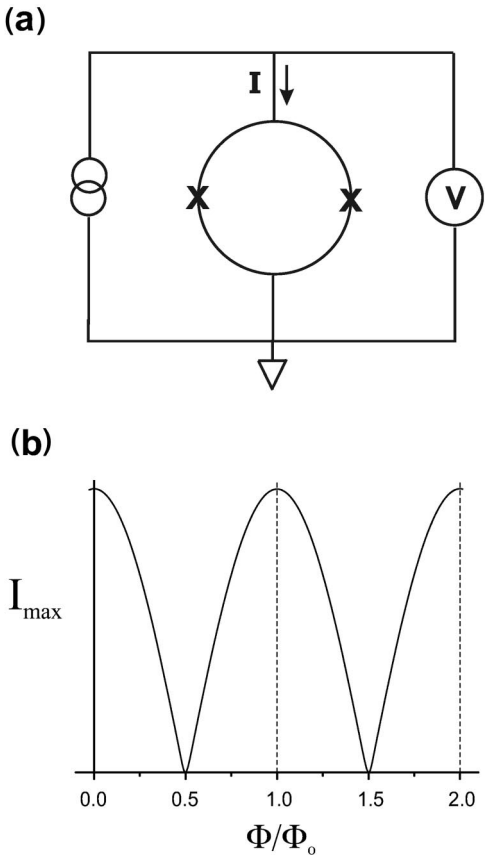

FIG. 2. The superconducting quantum interference device: (a) schematic representation of a superconducting dc SQUID; (b) a plot predicting the maximum dissipationless electrical current as a function of magnetic flux measured in units of the flux quantum.

$$I_{\max}=2I_c\left|\cos\left(\frac{\pi\Phi}{\Phi_0}\right)\right|. \tag{14}$$

The dc SQUID is the basis of the most sensitive detector of magnetic fields and has many important uses in science and technology. SQUID technology is reviewed in many sources (Van Duzer and Turner, 1981; Barone and Paternò, 1982; Likharev, 1986; Tilley and Tilley, 1990). To a large extent it is the technological importance of the SQUID (Clark, 1994) that has been a driving force toward fully understanding the many physical phenomena related to superconducting weak links.

IV. SUPERFLUID WEAK LINKS

A. Healing length

As mentioned above, weak coupling between two macroscopic quantum systems (describable by a scalar wave function) should lead to a sinelike current-phase relationship and all the associated phenomena seen in the superconducting systems. Superfluid helium is an obvious choice for another such system (Anderson, 1967). Because the helium mass is so much larger than the electron mass, it is unlikely that a true quantum tunneling junction can be created. However, as discussed below, it is possible to create the equivalent of a Dayem bridge by joining two bulk samples of superfluid via an aperture whose spatial dimensions are on the order of ξ.

In a mean-field theory of second-order phase transitions to superfluidity, for example, Ginzburg-Landau (Vollhardt and Wölfle, 1990) or Gross-Pitaevskii (Tilley and Tilley, 1990), the superfluid healing length can be estimated by the formula

$$\xi=\sqrt{\frac{\hbar^2}{2m\alpha}}, \tag{15}$$

where α is the coefficient of the superfluid condensation energy density term in the free-energy density. One can obtain α from measurements of temperature dependence of both the specific heat (on both sides of the transition) and the superfluid density (Tilley and Tilley, 1990).

For ^{4}He well below $T_\lambda\approx 2.17$ K, $\xi_4\sim 0.1$ nm, a dimension so small that fabrication of appropriate apertures has not yet been successful. However, very near T_λ, where ξ_4 diverges as $\sim(1-T/T_\lambda)^{0.67}$, the data from a recent experiment (Sukhatme *et al.*, 2001) exhibited hydrodynamic behavior that was interpreted by the authors as due to a sin ϕ current-phase relation. Considerable additional work will be required to determine if this assertion is correct.

For ^{3}He, which forms a superfluid in the millikelvin regime, Eq. (15) leads to (Vollhardt and Wölfle, 1990)

$$\xi_3=\frac{h\nu_f}{\pi\Delta}, \tag{16}$$

where ν_f is the Fermi velocity and $\Delta=1.76kT_c(1-T/T_c)^{1/2}$ is the energy gap. For the parameters relevant for liquid ^{3}He, $\xi_3(T=0)$ varies from 12 to 65 nm as the ambient pressure varies from 33 to 0 bars, respectively. This size scale is sufficiently large that nanofabrication techniques can be used to make apertures that might be characterized by the Josephson $I(\phi)$ relation, especially near the transition temperature at zero ambient pressure.

B. Possible weak-link geometries

Theoretical estimates of ^{3}He Josephson critical current densities are on the order of $\rho\Delta/p_F\sim 1$ kg m^{-2} s^{-1} (where Δ is the energy gap, p_F is the Fermi momentum, and ρ is the fluid density). Thus the critical mass current through a single aperture whose two transverse dimensions are close to the coherence length ($\sim$100 nm) would be on the order of 1×10^{-14} kg/s. Such mass currents are quite difficult to detect with a good signal-to-noise ratio. There are, however, at least two possible weak-link geometries that can allow for larger Josephson currents.

One possibility is to use a slit aperture for which only one transverse dimension is on the order of ξ. This has been the approach used by Avenel and Varoquaux at Saclay. In early experiments, ion milling techniques were used to create a (nominally 0.3×5 μm^2) slitlike structure in 0.2-μm-thick nickel foil (Varoquaux *et al.*, 1987). In

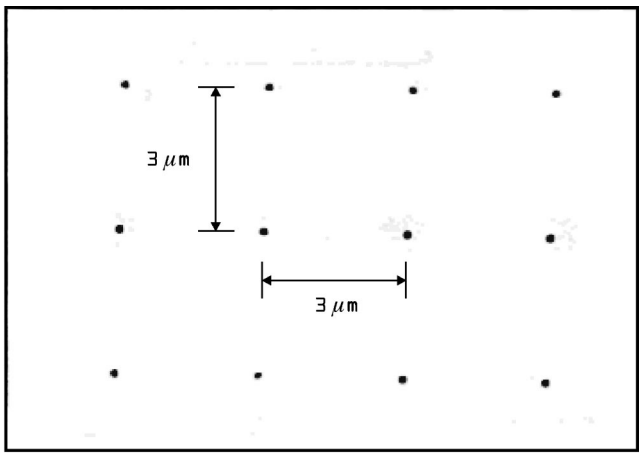

FIG. 3. A section of a nano-aperture array formed by etching through a ~50-nm-thick silicon nitride membrane (which is supported on a Si frame). The aspect ratio between the aperture diameter $d \approx \xi$ and the spacing $l = 3\ \mu$m is chosen such that $l \gg d$ to avoid series inductive effects.

later work, other slit apertures were fabricated in thin silicon nitride (Si_3N_4) membranes. Results from experiments using these slits are discussed extensively below.

Another approach, developed at Berkeley, uses an array of N nominally square nanoapertures etched through a thin silicon nitride (SiN) membrane. A scanning electron microscopy (SEM) picture of such an array is shown in Fig. 3. If an array behaves quantum coherently, then the Josephson mass currents will be N times greater, potentially yielding an adequate signal-to-noise ratio. One might expect that such coherence will exist because, if neighboring apertures are incoherent, there will be phase gradients along the membrane's surface. Such gradients involve additional energy, so the lowest energy state should favor coherence in an array.

On the other hand, thermal fluctuations could create incoherence among the apertures in an array. It is instructive to estimate the stochastic variations of phase difference (due to thermal fluctuations) that might exist across a volume of superfluid between two apertures spaced a distance L apart. Consider a square slab of area L^2 and thickness τ. The superfluid velocity is proportional to the gradient of phase:

$$v_s = \frac{\hbar}{2m_3} \nabla \phi. \tag{17}$$

Equating the kinetic energy in this volume $\frac{1}{2}\rho_s v_s^2 L^2 \tau$ to $\frac{1}{2}k_B T$, where ρ_s is the superfluid density, suggests that thermal energy could produce phase fluctuations between two apertures on the order of

$$\Delta\phi \approx \frac{2m_3}{\hbar}\sqrt{\frac{k_b T}{\tau \rho_s}}. \tag{18}$$

Taking a superfluid fraction of $\frac{1}{2}$, a temperature near 1 mK, and a slab thickness τ of ~100 μm gives us phase fluctuations due to thermal sources on the order of 2×10^{-4} rad. This small number suggests phase coherence will prevail in a ^{3}He nanoaperture array. Results from experiments in Berkeley with different types of nanoaperture arrays are discussed in detail below.

By contrast, since $\sqrt{T/\rho_s}$ is $\sim 3 \times 10^4$ greater in superfluid ^{4}He very close to T_λ, where the coherence length is comparable to presently feasible nanoapertures, such arrays are not expected from Eq. (18) to be coherent.

C. Theory of the weak-link current-phase relation

There are numerous theoretical predictions for the $I(\phi)$ relation for a ^{3}He weak link. The problem is challenging because the order parameter describing this superfluid is a complex 3×3 tensor quantity characterized by 18 parameters and because more than one superfluid phase exists. For a discussion of the full theoretical description of superfluid ^{3}He, see the comprehensive review by Vollhardt and Wölfle (1990). Reviews of related physics of Josephson weak links in unconventional superconductors can be found by Van Harlingen (1995) and Mineev and Samokhin (1999).

Because of this complexity, calculations to predict $I(\phi)$ for any real ^{3}He weak-link geometry require simplifying assumptions. Several researchers have used different theoretical techniques, forms for the order parameter, and boundary conditions. Here we briefly summarize the techniques and conclusions.

In their pioneering work on the Ginzburg-Landau description of superfluid ^{3}He, Ambegaokar, deGennes, and Rainer (1974) write down a simple weak Ginzburg-Landau coupling between two samples of superfluid. They conclude that, if the superfluid is axial (e.g., A phase), then there are two possible current-phase relations. One is conventional, i.e., $I \propto \sin(\phi)$, when the $\boldsymbol{l}$ vectors are parallel on both sides of the weak link. When the $\boldsymbol{l}$'s are antiparallel, there is zero Josephson current (to first order).

Kopnin (1986) considered the case of an orifice whose diameter and length are much smaller than the healing length. Using semiclassical Green's-function techniques and considering temperatures only near T_c, he derived the current-phase relation for two different situations. When the scattering near the aperture is diffuse, $I(\phi)$ was found to be sinelike with the magnitude of I_c proportional to $(1 - T/T_c)^2$, whereas when scattering is specular $I(\phi)$ is still sinelike, but now I_c is proportional to $1 - T/T_c$.

Monien and Tewordt (1986, 1987) used a Ginzburg-Landau representation of the free energy of the weak link and calculated the current through an aperture for a fixed phase difference across it. Different assumptions for the form of the order parameter were made and specular scattering boundary conditions chosen. A variety of predictions for $I(\phi)$ resulted, with many having multivalued and noncontinuous functional forms.

Hook (1987) studied $I(\phi)$ in a superfluid phase containing a single order parameter (S wave) as a function of the length and diameter of the aperture using the Ginzburg-Landau formalism. The phase diagram of phenomena occurring in the aperture was then mapped out in the plane whose axes are aperture length l and diameter d. When $l \ll \xi$ and $d \ll \xi$, a sinelike $I(\phi)$ resulted. If

both $l \gg \xi$ and $d \gg \xi$, the phenomenon predicted was 2π phase slippage.

Kurkijärvii (1988) studied theoretically an aperture whose diameter and length are much smaller than ξ, with specular scattering at the walls. This is often referred to as the "pinhole" limit. Both the A phase and B phase were considered in calculations using the quasiclassical Green's-function approach. In the A phase, for $\boldsymbol{l}$ vectors parallel on the two sides of the aperture, $I(\phi)$ is predicted to be sinelike, while opposite $\boldsymbol{l}$ vectors produce a zero Josephson current. For the B phase near T_c, a sinelike $I(\phi)$ is predicted, but for very low temperatures this relationship is skewed and finally becomes proportional to $\sin(\phi/2)$.

Thuneberg (1988) used numerical solutions of the Ginzburg-Landau equations in a two-dimensional model of a weak-link aperture in the B phase. The current-phase relation is found to be sinelike if the **n** vectors of the B-phase order parameter are parallel. Antiparallel **n** vectors resulted in the prediction of skewed and discontinuous $I(\phi)$ functions.

Ullah and Fetter (1989) also used numerical solutions to the Ginzburg-Landau equations in two dimensions. Boundary conditions specifying the phase gradient, rather than the phase, at the bulk ends of the aperture were used. They computed the critical current as a function of the width and length of the weak link.

Thuneberg, Kurkijärvii, and Sauls (1990) used the quasiclassical theory to study the case of different-shaped apertures in thin walls ($d \ll \xi$) with specular scattering. The effects of a finite-size radius aperture on the order parameter and Josephson current, and a comparison with the pinhole result in the infinitely thin wall (Kurkijärvii, 1988), are also discussed (Thuneberg *et al.*, 1990).

Very recently, a comprehensive theoretical analysis of the ^{3}He weak-link problem in superfluid ^{3}He has been carried out by Viljas and Thuneberg (2002). These authors discuss the current-phase relationships of weak links between two volumes of superfluid using an approach that is divided into mesoscopic and macroscopic components. This is done to allow for analysis of effects of texture on $I(\phi)$. The weak link is assumed to be a pinhole. Using a self-consistent order parameter and quasiclassical techniques they calculate the current-phase relationship for several cases. In the isotextural case, $I(\phi)$ is calculated assuming a constant spin-orbit texture. In the opposite anisotextural case, the texture changes as a function of the phase difference and its stiffness is considered as well.

Theoretical work specifically focused on the special case of the "π state" [and its associated $I(\phi)$] is reviewed in Sec. IX below.

The theoretical analyses of this challenging and complex problem have resulted in the prediction of a wide variety of current-phase relations as a function of geometry, superfluid phase, texture near the weak link, magnetic field, and temperature. It has remained an experimental challenge to determine the actual $I(\phi)$ of ^{3}He weak links.

V. EXPERIMENTAL TECHNIQUES

Superfluid ^{3}He exists only at temperatures below a few millidegrees Kelvin. The transition temperature T_c varies from 0.9 mK at $P=0$ to 2.7 mK near the solidification pressure of 30 bars. Thus the superfluid Josephson weak-link experiments must be performed using millikelvin refrigeration techniques. Usually the cooling is performed using adiabatic demagnetization of the nuclear spins in several kilograms of copper metal (Lounasmaa, 1974; Richardson and Smith, 1988; Pobell, 1992).

To study superfluid ^{3}He weak links, one needs to apply and measure chemical-potential differences and mass currents in a fashion analogous to the application and measurement of voltage differences and electrical currents in superconductors. Because the apertures are necessarily on the submicron scale (i.e., on the order of the coherence length), the mass currents are small, and thus specialized techniques have been developed to measure mass currents and to control chemical-potential differences.

For a fluid, chemical-potential variations are given by (Khalatnikov, 1965)

$$d\mu = \frac{m\,dP}{\rho} + s\,dT, \tag{19}$$

where m is the particle mass, P is the pressure, ρ is the density, s is the entropy per particle, and T is the temperature. In all the ^{3}He weak-link experiments thus far, the temperature variation term has been negligible. In that case, the chemical-potential difference between two superfluid ^{3}He samples is given by

$$\Delta\mu = \frac{2m_3\Delta P}{\rho}, \tag{20}$$

where the factor of 2 reflects the Cooper-paired nature of the superfluid ^{3}He "particles."

The key element used for control and measurement of pressure difference is a flexible membrane coated with a metallic film, as shown schematically in Fig. 4. A rigid electrode adjacent to the membrane can be used to apply electrostatic pressures to the system. Small displacements (from equilibrium) of the membrane are linear in the applied pressure difference. For a given applied voltage V, the membrane's (spatially averaged) equilibrium displacement x_{eq} is determined by the balance between its spring force and the electrostatic pressure:

$$x_{\mathrm{eq}} = \frac{1}{2}\frac{A\varepsilon V^2}{kd^2}, \tag{21}$$

where ε is the permittivity of the liquid, A is the area of the membrane, k is the membrane spring constant, and d is the spacing between the membrane and rigid electrode. For typical membranes used in the superfluid aperture experiments, $A \sim 10^{-4}$ m^2, $V \sim 10^2$ V, $k \sim 3 \times 10^3$ N/m, and $d \sim 5 \times 10^{-5}$ m, resulting in typical displacements of order 1 μm. The instantaneous pressure difference across the membrane (and thus across the aperture) is given by

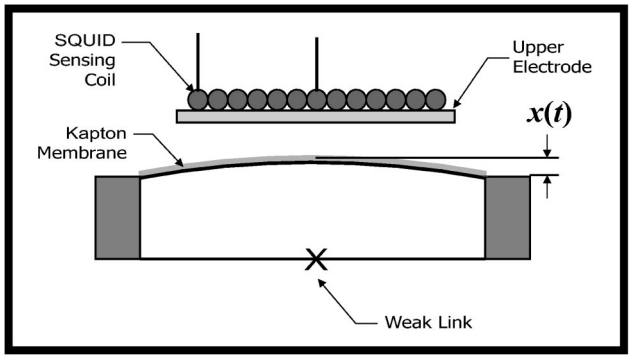

FIG. 4. A typical experimental arrangement used to probe the properties of superfluid weak links. An inner volume is bounded by an impermeable, rigid frame that supports a flexible membrane. The fluid within is coupled to an outer volume of fluid through the weak link under study. The membrane is superconducting and faces an adjacent solid electrode and an input coil to a superconducting displacement sensor. This membrane serves as a pressure gauge, a mass current meter, and a source of chemical-potential difference (i.e., pressure differential). The displacement from equilibrium $x(t)$ is shown.

$$\Delta P(t)=\frac{k}{A}[x(t)-x_{\rm eq}]=\frac{k}{A}\Delta x(t), \tag{22}$$

where $\Delta x(t)$ is the instantaneous displacement from equilibrium. For the parameters listed here, differential pressures of the order of 10 Pa and smaller are typical. In the analyses below we set $x_{\rm eq}$ equal to 0 unless explicitly stated otherwise.

A flexible membrane can also be used to measure mass currents. Referring to Fig. 4, we see that any fluid entering through the aperture will increase the internal volume by displacing the membrane. Assuming an incompressible fluid, the mass current is given by

$$I=\rho A\dot{x}, \tag{23}$$

where ρ is the fluid density.

Since the membrane position x yields the pressure [Eq. (22)] and $\dot{x}$ yields the current [Eq. (23)], the key to studying properties of flow through small apertures is to use a highly sensitive displacement transducer to monitor $x(t)$. An appropriate technique was developed by Paik (1976) in the context of displacement measurements for gravity-wave antennae and adapted for use with superfluid helium by Avenel and Varoquaux (1986). The Paik sensor is based on the small changes in the mutual inductance between a pancake-shaped superconducting coil and a superconducting plane, when that plane moves with respect to the coil. A persistent current is trapped in the pancake coil, which is also connected to the input coil of a dc SQUID. A change in mutual inductance results in a SQUID signal $V_{\rm sq}$ proportional to x.

The ultimate displacement noise floor is determined by the flux noise level in the SQUID and is usually optimized by having the spacing between pancake coil and membrane be as small as possible. In nanoaperture experiments one can achieve a displacement noise $\delta x \approx 10^{-15}$ m/$\sqrt{\rm Hz}$ for operating frequencies up to $\sim$10 kHz when the spacing is $\sim$100 μm.

In fact, it is rather rare to be limited by the electronic noise in the SQUID readout. Local vibrations of the experimental apparatus typically move the membrane for a variety of reasons and produce a "noise" signal in excess of the intrinsic electronic SQUID noise. For this reason sophisticated vibration isolation and acoustic shielding (Avenel *et al.*, 1993) are usually required to obtain a good signal-to-noise ratio when determining ^{3}He Josephson mass current signals.

VI. EQUATION OF MOTION FOR ϕ IN A MEMBRANE-APERTURE CELL

The general motion of a flexible membrane coupled to a $\sin\phi$ weak link is similar to that of a rigid pendulum. Since the pressure ΔP across the weak link is proportional to the membrane displacement [Eq. (22)], Eq. (8) becomes

$$\dot{\phi}=-\frac{2m_3}{\rho\hbar}\frac{k}{A}[x(t)-x_{\rm eq}]. \tag{24}$$

Differentiating gives

$$\ddot{\phi}=-\frac{2m_3}{\rho\hbar}\frac{k}{A}\dot{x}=-\frac{2m_3kI_c}{\hbar\rho^2A^2}\sin\phi=-\omega_p^2\sin\phi, \tag{25}$$

where we have used the fact that the current is $I=\rho A\dot{x}=I_c\sin\phi$. Equation (25) is the equation of motion for the quantum phase evolution when dissipation is ignored. It is identical in form to the equation of motion for a rigid pendulum whose small-oscillation frequency is ω_p, if ϕ now represents the angular displacement from the vertical.

There are three characteristic motions of a rigid pendulum, as indicated schematically in Figs. 5(a)–5(d). For small displacement angles, $\sin\phi\approx\phi$ and the motion of ϕ and $\dot{\phi}$ is simple harmonic with frequency ω_p. For large-angle displacements with $\phi<\pi$, the oscillator is nonlinear with frequency approaching zero as the angular amplitude approaches π (Monien and Tewordt, 1987). Furthermore, as ϕ approaches π, $\ddot{\phi}$ approaches zero and $\dot{\phi}$ remains near zero for relatively long periods of time. For very large energies ϕ grows without limit, while $\dot{\phi}$ oscillates about a nonzero value as the pendulum orbits about the suspension point. Starting with a large initial energy, if there is slight dissipation, the oscillator motion evolves through each of these stages in turn, ending in the simple pendulum mode.

The important dynamical variable in weak-link experiments using a membrane-aperture cell is the quantum phase difference ϕ, which, after an initial large energy input (e.g., a large pressure step), evolves through three stages equivalent to those in the rigid pendulum dynamics. The observable in cells such as those in Fig. 4 is the membrane displacement $\Delta x(t)$, which from Eq. (24) is proportional to $\dot{\phi}$. Therefore, to compare theory

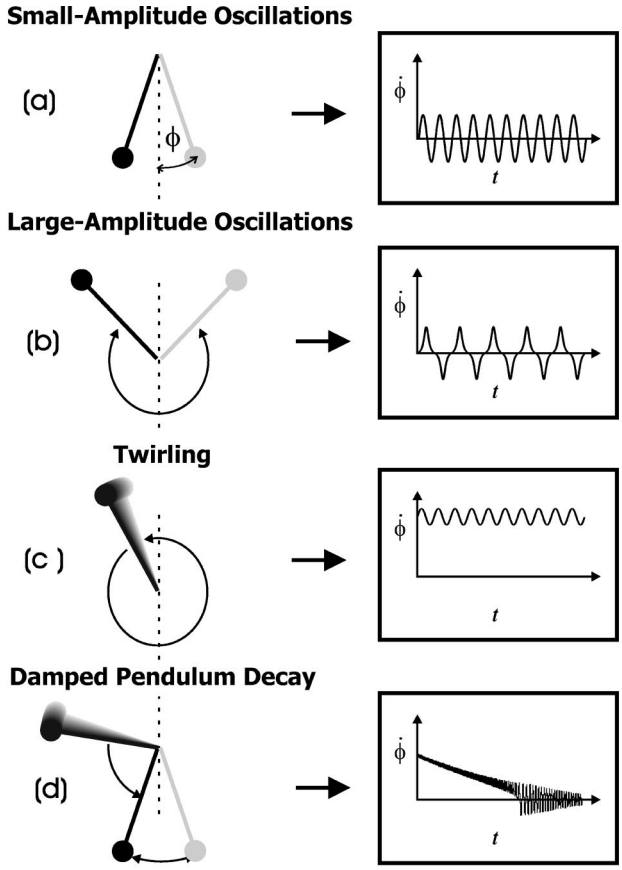

FIG. 5. Rigid pendulum motion: (a) small-amplitude motion, a simple pendulum; (b) motion approaching $\phi \approx \pi$, a nonlinear oscillator that spends a significant fraction of the cycle near $\dot{\phi} \approx 0$; (c) continuous twirling at some frequency resulting from a large initial energy. The mean value of $\dot{\phi}$ is not zero; (d) transient decay with slight damping. When $\langle \dot{\phi} \rangle \neq 0$, the twirling frequency is proportional to $\langle \dot{\phi} \rangle$.

and experiment, it is the dynamics of $\dot{\phi}$ that is the focus of attention, and the characteristics of $\dot{\phi}$ in each example of these dynamics are shown in the right-hand panels of Fig. 5. We show in Fig. 5(d) a numerical simulation of both ϕ and $\dot{\phi}$ when the system has large initial energy and small damping. The twirling motion of the pendulum discussed above is equivalent to an oscillation of x in the membrane-aperture cell. Careful inspection of the figure would reveal that the frequency of these oscillations is proportional to the average displacement of x from equilibrium.

VII. SUPERFLUID JOSEPHSON OSCILLATIONS

A. Josephson oscillations

The most striking phenomenon characteristic of the $\sin \phi$ current-phase relation is a spectrally pure oscillating current associated with a constant chemical-potential difference. This violates our classical intuition that a pressure head applied across the fluid in a hole should result in unidirectional flow.

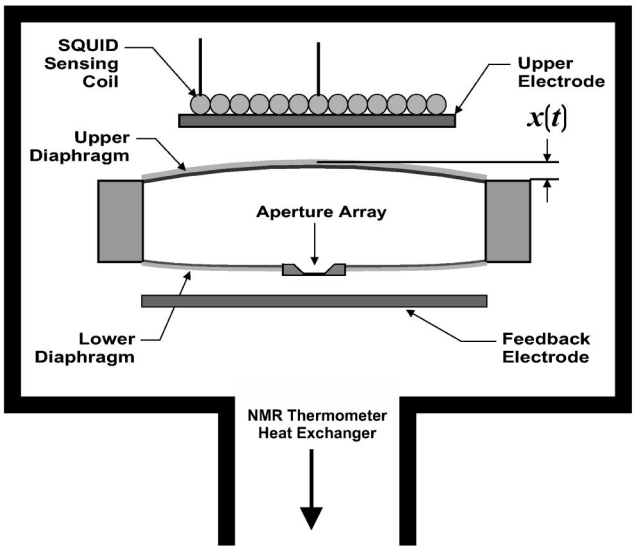

FIG. 6. The Berkeley double-diaphragm cell. The addition of a second (lower) membrane with another adjacent electrode permits one to use feedback to drive flow at a constant pressure differential.

For ^{3}He the Josephson frequency relation equivalent to Eq. (10) is given by

$$\omega_J \equiv \frac{\Delta\mu}{\hbar} = \frac{2m_3 \Delta P}{\rho\hbar}. \tag{26}$$

Thus, for example, a pressure head of 1 Pa applied across a superfluid Josephson weak link should create an oscillating mass current of amplitude I_c at a frequency of 187.4 kHz. The Josephson oscillations resulting from a given pressure head correspond to the twirling mode of the pendulum [Fig. 5(c)].

A mass current oscillating at frequency ω through an aperture of area σ will result in an amplitude x_0 of membrane motion given by

$$x_0 = \frac{j_c \sigma}{\rho A \omega}, \tag{27}$$

where j_c is the Josephson critical current density (I_c/σ). Since theoretical estimates suggest that $j_c \sim 1$ kg m^{-2} s^{-1}, for an aperture of diameter $\sim \xi_3$ and a Josephson frequency of 100 Hz, this would result in an oscillation amplitude of membrane motion $\sim 3 \times 10^{-15}$ m, barely within the range of detectability. However, as noted above, a coherent array of M nanoapertures should in principle make these oscillations signals M times greater and hence detectable.

These Josephson oscillations have been observed in nanoaperture arrays using an experimental cell similar to that shown schematically in Fig. 6. The cell consists of a very short cylindrical container bounded on the top and bottom by flexible Kapton® membranes. Both membranes are metal coated, the top with a superconducting film and the bottom with a normal metal. Electrodes are placed outside the cylinder, both above and below. These electrodes are used in conjunction with voltage supplies and capacitance bridges to apply pres-

sure heads to the cell and to determine the spring constant of the membranes. The input coil of a Paik displacement sensor is positioned above the top membrane. A nanoaperture array is built into the lower membrane.

In one type of experiment using an array [65×65 apertures, 100 nm diameter, micromachined (Amar, 1993) in a 50-nm-thick silicon nitride membrane], a voltage step is applied between one of the membranes and its adjacent electrode. The pull on the membrane creates a pressure difference ΔP [and therefore a chemical-potential difference given by Eq. (20)] across the nanoaperture array. As described by Eq. (26), this should lead to oscillating currents at the frequency

$$f_j = \frac{2m_3 P}{\rho h} = 187.4 \text{ kHz/Pa}. \tag{28}$$

As shown in Eq. (27), the displacement amplitude of the detector membrane is inversely proportional to the frequency. Therefore the range of pressure differential must be chosen to limit the predicted Josephson frequency to values sufficiently small to permit detection. The pressure differentials are typically in the millipascal regime, and the Josephson oscillation signal is in the audible region. Under these conditions Josephson oscillations are indeed observed (Pereverzev *et al.*, 1997). In fact, the first detection of Josephson oscillations was made by listening to the voltage output of the SQUID with a set of audio headphones.

After the application of a step voltage, the output of the SQUID displays a relaxation transient $x(t)$ as the membrane relaxes to a new equilibrium position in a time scale of several seconds. The SQUID output signal applied to audio headphones reveals an oscillation signal in the audio range, which sweeps downward in frequency as the pressure head decays due to dissipative processes (Simmonds, Marchenkov, Vitale, *et al.*, 2000).

When the recorded SQUID signal is Fourier transformed in each small time interval of the transient, it displays a clear peak. Since the average displacement of the membrane measures the pressure difference [from Eq. (22)], one can plot the frequency of the fast Fourier transform (FFT) peak in each time interval as a function of the pressure across the array at the same instant. The result can be seen in Fig. 7.

All the data points, from several different temperatures, lie on the same straight line, whose slope is given within systematic error by the Josephson frequency formula, Eq. (28). At temperatures near T_c, where the healing length is long, the FFT's reveal only the Josephson frequency (i.e., no higher harmonics) consistent with a pure $\sin\phi$ current-phase relation. At lower temperatures, higher harmonics can be detected.

Although, as shown below, there are several other observed phenomena characteristic of a $\sin\phi$ current-phase relation, the observation of dc pressure-driven single-harmonic Josephson oscillations is still the simplest and clearest manifestation of a superfluid Josephson weak link.

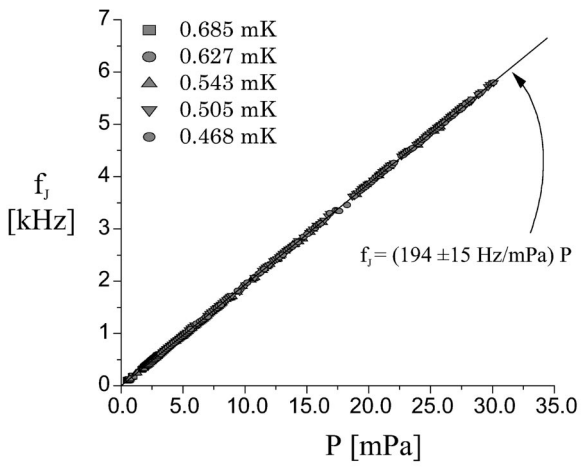

FIG. 7. A plot of the frequency of membrane oscillations versus the differential pressure for several different temperatures. All the points lie on a universal line that is consistent with the prediction of Eq. (28).

B. Quantum pressure standard and phase meter

The data shown in Fig. 7 permit one to make an *in situ* absolute pressure calibration of the displacement transducer. The pressure scale used in the figure was based on an electrostatic calibration (i.e., the relation between the SQUID output and the pressure created by the application of a voltage) that is subject to systematic error on the order of 10%. However, by assuming the correctness of the superfluid Josephson frequency formula [Eq. (28)], one can establish an absolute calibration of the pressure scale. Since pressure is a linear function of average displacement, which is itself a linear function of the SQUID signal $V_{\rm sq}$, one can write from Eq. (26)

$$\Delta P = \beta V_{\rm sq} = \frac{\rho\hbar\omega_J}{2m_3}, \tag{29}$$

where β is the unknown calibration constant. The slope of a plot of $V_{\rm sq}$ vs ω_j then yields β, thus providing an absolute quantum pressure standard.[1] This is analogous to the definition of the standard volt (Taylor *et al.*, 1969; Pöpel, 1992) in terms of Eq. (10).

The establishment of this absolute pressure scale provides a technique for determining the instantaneous quantum phase difference, which is of great utility for exploring the physics of superfluid weak links. Equation (7) links the instantaneous phase difference to an integral of the chemical-potential differential, which is established by the pressure head through Eq. (20). Following some excitation of the aperture-membrane oscillator, a continuous determination of $\phi(t)$ may be made by integrating the time-dependent SQUID voltage $V_{\rm sq}$:

[1]In order to create a very precise quantum pressure standard based on the superfluid Josephson frequency relation, one would need to determine the fluid density to greater accuracy than known at present.

$$\phi(t)=\phi_0-\frac{1}{\hbar}\int_0^t(\mu_2-\mu_1)dt'$$
$$=\phi_0-\frac{1}{\hbar}\int_0^t\frac{2m_3}{\rho}\Delta P dt'$$
$$=\phi_0-\frac{2m_3\beta}{\rho\hbar}\int_0^t V_{\rm sq}(t')dt'. \quad (30)$$

We assume that, when the system is stationary, $\phi_0=0$ and ignore inertial terms that can be shown to be typically no greater than 1%. Implementation of Eq. (30) results in a continuous measurement of the quantum phase difference, i.e., a "phase meter."

VIII. DETERMINATION OF THE CURRENT-PHASE RELATION $I(\phi)$

According to the simple arguments leading to Eq. (5), the $I(\phi)$ relation should be sinelike for sufficiently weak coupling between superfluid reservoirs. However, as discussed in Sec. IV.C, detailed calculations for ^{3}He do not always lead to this simple result. Therefore it has been of great interest to determine $I(\phi)$ for a ^{3}He weak link as a function of temperature and pressure. There have been several experimental approaches to this challenge.

A. Method I

The first approach for probing nonlinear current-phase relations was suggested by Zimmermann (Brooks *et al.*, 1979) in the context of vortex phase slippage in ^{4}He. The method focuses on the dynamical behavior of a single aperture [whose $I(\phi)$ one wishes to know] shunted by a larger tube. This shunted-aperture arrangement has been used with great success, especially at Saclay, for the study of vortex creation in ^{4}He (Avenel and Varoquaux, 1985; Varoquaux *et al.*, 1986; Avenel *et al.*, 1990; Zimmermann *et al.*, 1990; Ihas *et al.*, 1992; Varoquaux *et al.* 1993).

In superfluid ^{3}He, this topology was first applied by Parpia and Reppy (1979) who used a superfluid-filled torus, which played the role of the shunt tube, interrupted by a wall containing a micron-scale aperture. The torus was the inertial element in a torsional oscillator. They studied the oscillator response to an ever-increasing driving force in search of nonlinear behavior which would result from a sinelike current-phase relation in the aperture. Although this experiment did not reveal any simple signatures, the oscillator exhibited nonlinear chaotic behavior under certain conditions. In hindsight, this may have been an effect due to a weak-link $I(\phi)$ function that was approaching the Josephson $\sin\phi$ limit. However, without the foundation of simpler effects to build on, the chaotic signatures could not be analyzed as a manifestation of Eq. (5).

The first convincing experimental evidence for a sinelike $I(\phi)$ in superfluid ^{3}He was reported by Avenel and Varoquaux (1988). This team studied the shunted-aperture topology but now coupled to a membrane

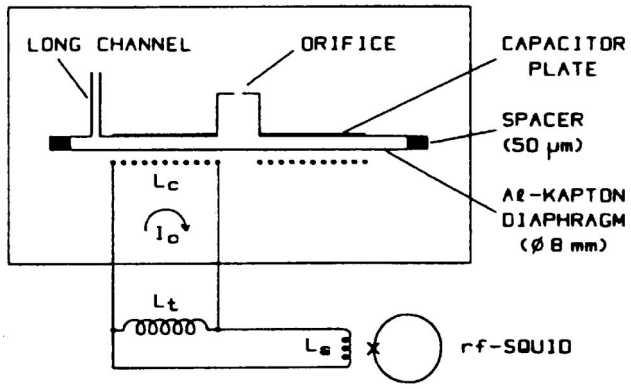

FIG. 8. The geometry of the Saclay cell. An inner volume is enclosed by rigid walls and a flexible membrane. The walls include a small slit orifice (the weak link) as well as a larger cross-section parallel channel of known length and width. The parallel channel shorts out dc pressure differentials but permits circulation changes in the closed path that passes through both the channel and orifice. The position of the membrane is monitored by a SQUID displacement detector.

(Brooks *et al.*, 1979). The weak link was nominally a slit of approximate dimensions $0.3\times5\ \mu$m^2. Figure 8 is a schematic representation of their original cell. As explained in Appendix A, the membrane can be represented by an effective capacitance, and the two parallel flow paths can each be characterized by a representative kinetic inductance. The cell in the figure is equivalent to a combination of capacitor and inductor and thus exhibits hydrodynamic resonance. However, the inductance of the weak link can be a function of the phase difference across it (as discussed in Appendix A) and thus the equivalent oscillator is nonlinear as a function of its amplitude.

Avenel and Varoquaux analyzed the oscillator dynamics by parametrizing the aperture $I(\phi)$ using a model introduced by Deaver and Pierce for superconductors. In this model the slit aperture is assumed to be a linear inductance in series with a sinelike weak link. This leads to a parametrization of the current-phase relation given by

$$I=I_c\sin\zeta,$$

where

$$\phi=\zeta+\alpha\sin\zeta. \quad (31)$$

As shown schematically in Fig. 9(a), ϕ is the real phase drop across the combined system, while ζ is the (unmeasurable) phase drop across the sinelike element. In this model, α is the ratio of the inductance of the series' linear element to the inductance of the weak link at zero phase bias. For $\alpha=0$ the model represents a pure sinelike weak link, whereas for $\alpha>1$ it represents an $I(\phi)$ that is a multivalued function. Figure 9(b) shows a plot of $I(\phi)/I_c$ for various values of α. The oscillator's equation of motion involves both α and I_c.

The amplitude of the oscillator in Fig. 8 was measured as a function of driving force and frequency (Avenel and Varoquaux, 1988; Varoquaux *et al.*, 1992). Figure 10 displays a response characteristic for the B phase of ^{3}He at

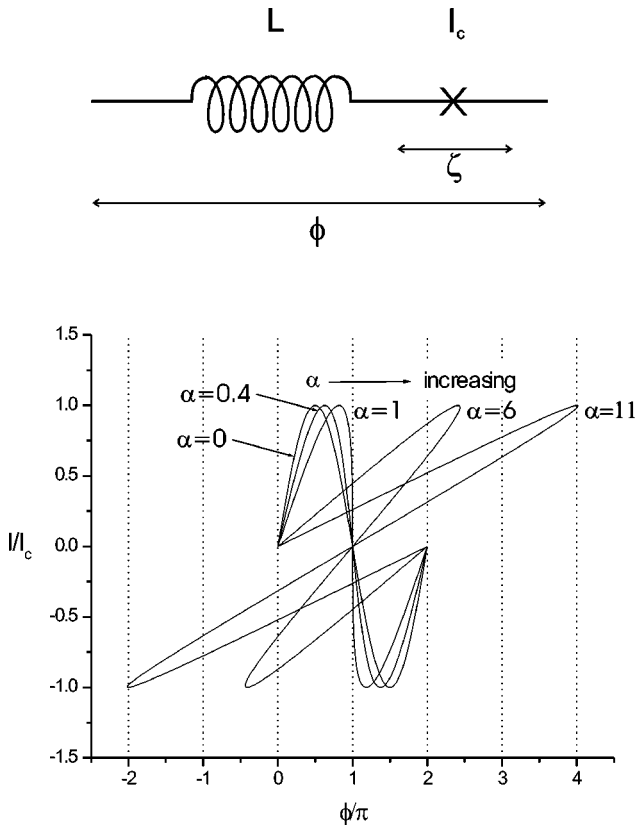

FIG. 9. Plotted values of the normalized Deaver-Pierce current-phase relation for various values of α. When $\alpha<1$, the curve is single valued, whereas when $\alpha>1$, it becomes triple valued and hysteretic.

zero pressure. It shows a plot of the peak amplitude of motion of the oscillator. The solid line is a best fit from a numerical simulation of the experiment letting both α and I_c vary as fitting parameters. Because a fit to the data can be achieved by using a sinelike current-phase relation, this is the first experimental result consistent with the existence of a Josephson weak link in superfluid helium.

Table 1 from Varoquaux *et al.* (1992) gives the best-fit values of α and R at three temperatures where a good fit to the numerical model could be achieved and one lower temperature where the fit was difficult. For temperatures above $0.83T_c$, $\alpha<1$, indicating that the aperture is getting close to a sinelike $I(\phi)$ function.

As a further indication of the form of $I(\phi)$, the authors point out that on some occasions the driving force on the membrane results in no fluid flow through the parallel aperture and tube. As discussed in Appendix A, for a weak link characterized by a function $I(\phi)$, the equivalent kinetic inductance is given by

$$L_w(\phi)=\frac{\kappa_3}{2\pi}\left(\frac{dI}{d\phi}\right)^{-1}. \tag{32}$$

The absence of flow in response to an applied pressure implies that the parallel combination of the shunt inductance L_s and L_w,

$$L_p=L_sL_w/(L_s+L_w), \tag{33}$$

behaves as an infinite inductance. Since the parallel shunt tube is a simple positive linear inductance, the aperture must therefore have a negative inductance equal in magnitude. Such a situation could occur if there is permanent π phase bias across the aperture and if the slope of $I(\phi)$ at π is sufficiently large and negative. This is a property of a sine function.

Figure 11 shows a plot of $I(\phi)$ derived from Eq. (31) using the reported fit parameters in Table 1 of Varoquaux *et al.* (1992). Although this parameter-fitting method suggests a sinelike $I(\phi)$ at high temperatures, the rapid variation in I_c with temperature is consistent neither with existing theories nor with subsequent measurements on weak-link arrays to be discussed below. As the authors commented (Varoquaux *et al.*, 1992), further progress in understanding the $I(\phi)$ in detail requires " . . . a direct measurement of $I(\phi)$ which in turn implies a modification of the apparatus to directly monitor ϕ."

This method of fitting a numerical simulation to the data was applied to the study of both *A* and *B* phases of ^{3}He at elevated pressures (Avenel and Varoquaux, 1989). In this regime the aperture was mostly characterized by a linear inductance exhibiting phase slippage. No striking difference was observed between the two phases. This could reasonably be interpreted as evidence that, at elevated pressure, the coherence length is considerably smaller than the apertures used and thus the apertures would not be expected to be in the sin ϕ Josephson regime.

B. Method II

An alternative approach to method I was developed at Berkeley (Backhaus *et al.*, 1997; Marchenkov *et al.*, 1999) based on the establishment of the *in situ* quantum pressure standard and the phase meter as described by Eq. (30).

The experimental cell in Fig. 6 can be operated in several different modes. We mentioned in Sec. VI that the solution of Eq. (24), the equation of motion for ϕ, exhibits nonlinear oscillations around equilibrium analogous to rigid pendulum motion, and we pointed out that the observable $x(t)$ is analogous to $\dot{\phi}$. If the membrane is displaced far from equilibrium (by application of a voltage on the nearby electrode) and then released, the position $x(t)$ should relax towards equilibrium with a characteristic transient behavior similar to that shown in Fig. 5(d). When the membrane reaches its equilibrium position, the fluid inertia in the array causes it to overshoot and then oscillate about equilibrium. This is equivalent to the instant when dissipation in the analogous pendulum causes the twirling motion to cease and nonlinear oscillation about equilibrium to commence, as discussed in Sec. X.

The end of a typical transient is shown in Fig. 12. This compares very well with the solution of Eq. (25) with small damping, shown in Fig. 5(c). Since $V_{\rm sq}(t)$ is linear in $x(t)$, the mass current can be determined at every instant in time from $dV_{\rm sq}/dt$,

$$I(t)=\rho A\dot{x}(t)=\rho A\,\gamma(dV_{\rm eq}/dt), \tag{34}$$

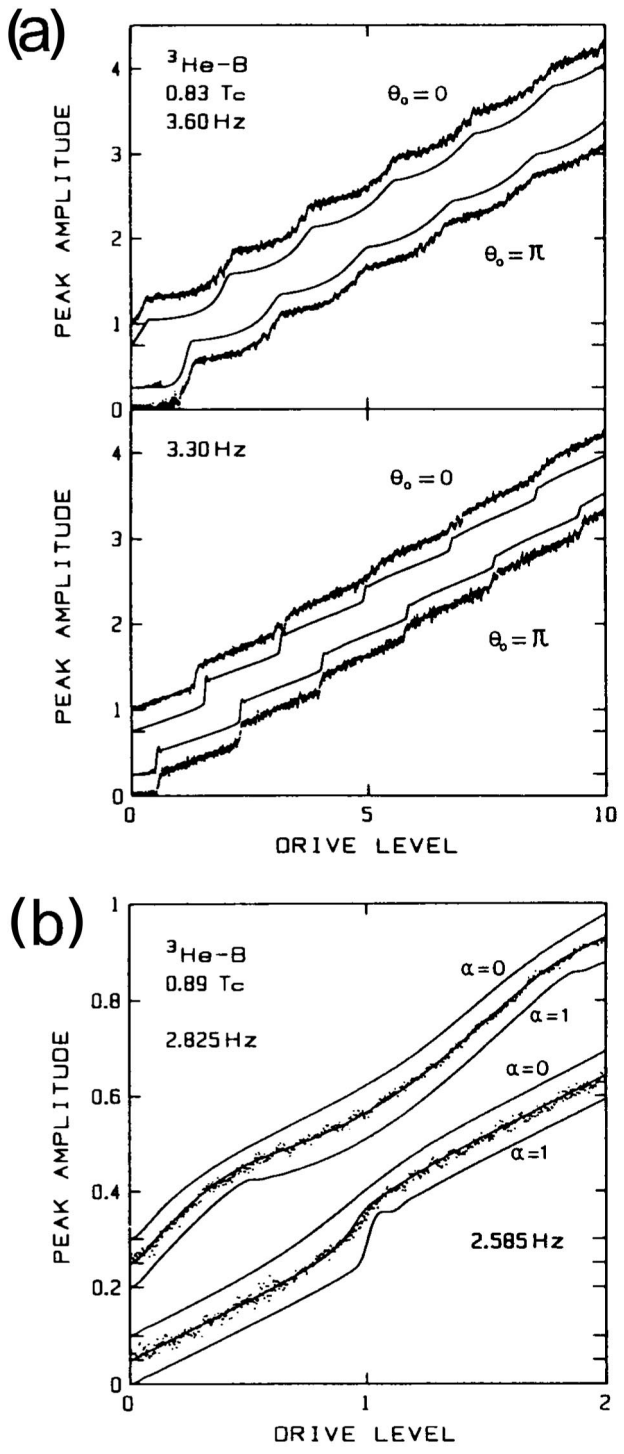

FIG. 10. Staircase patterns in superfluid ^{3}He: (a) Data from Saclay (Avenel and Varoquaux, 1988; Varoquaux *et al.*, 1992) displaying staircase patterns at $0.83T_c$. The smooth curves are staircases simulated numerically using the Deaver-Pierce current-phase model. The two sets of data represent different extremes of trapped phase bias. (b) A section of one of the staircases showing the changes in the simulation for different values of the α parameter. In the top curve, $\alpha=0.4$ is a best fit.

where γ is determined by an electrostatic calibration procedure.

Using Eq. (30) one can integrate the same data stream, $V_{\rm sq}(t)$, to give the instantaneous phase $\phi(t)$. By eliminating the common time variable between $I(t)$ and $\phi(t)$, one can generate the function $I(\phi)$. No fitting parameters are required.

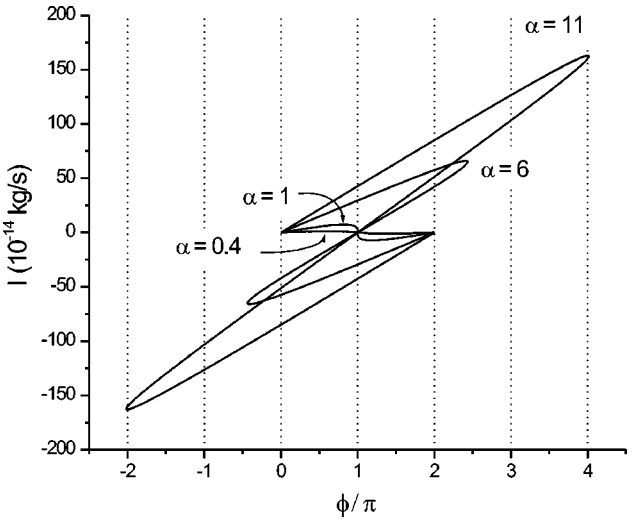

FIG. 11. The current-phase relations deduced from method I using the parameters determined at Saclay (Varoquaux *et al.*, 1992).

The measured $I(\phi)$ functions for a nanoaperture array (Marchenkov *et al.*, 1999) for various temperatures are shown in Fig. 13. $I(\phi)$ is sinelike at higher temperatures (above $\sim 0.65T_c$), the region where ξ is large. As the temperature is lowered, the sine function evolves, with the slope at π decreasing, eventually changing sign (negative to positive). At the lowest observed temperature the function appears almost proportional to $\sin 2\phi$.

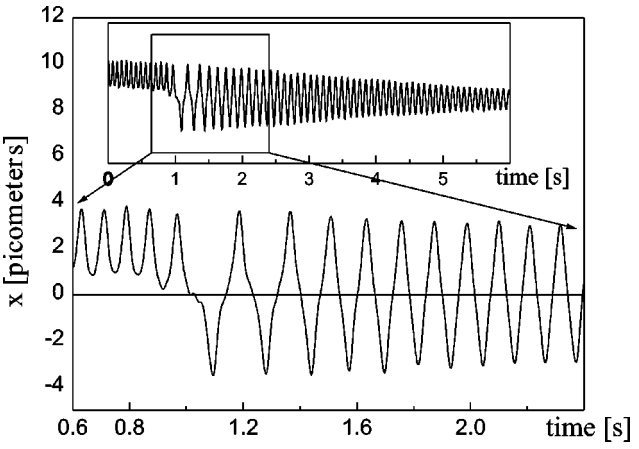

FIG. 12. The SQUID signal showing the upper membrane displacement approaching the end of a transient. The transient was initiated by applying a step increase in voltage between the membrane and the adjacent electrode. For $t<1$ s, the system displays Josephson oscillations (twirling motion in the pendulum), while the mean pressure differential is positive. When the average pressure falls to zero, the system at first exhibits nonlinear pendulum oscillations about the final equilibrium position. At later times and smaller amplitudes, the motion is harmonic. The mechanisms that contribute to the energy dissipation are discussed later in the paper.

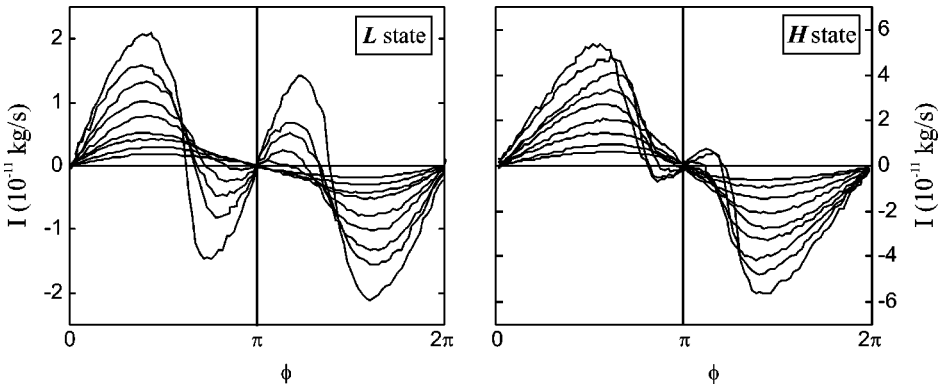

FIG. 13. Current-phase relations determined by method II at a variety of temperatures. The curves represent equal temperature intervals of $0.05T_c$ beginning at $0.45T_c$ with the largest critical current. The fact that there are two sets of curves is discussed in Sec. IX.A.

For several reasons, the Deaver-Pierce model [Eq. (31)] cannot be used to represent the form of many of the directly measured $I(\phi)$'s displayed in Fig. 13. For example, in the Deaver-Pierce parametrization, when $\alpha > 1$, the $I(\phi)$ curves are triple valued near π, but none of those in Fig. 13 are. Also, in the Deaver-Pierce parametrization $I(\phi)$ does not cross the zero-current line at any point where $\phi < \pi$, but many of the $I(\phi)$ curves in Fig. 13 do. Since the Deaver-Pierce parametrization used in method I is a good fit to the data for α up to 6 (Varoquaux *et al.*, 1992), one must ask how to reconcile that observation with the $I(\phi)$ curves displayed in Fig. 13. One possibility is that $I(\phi)$ in the single slit used in the Saclay experiments may be quite different from that of an array of apertures. Geometrically, the dimensions of the elementary aperture in the array ($100 \times 100\,\mathrm{nm}^2$) are far smaller than the maximum dimension of the slit (5 μm). Another possibility, as pointed out by those authors, is that the curve-fitting method is "likely to be insensitive to the detailed shape of the current-phase relation." It may be that the fit of the data to the Deaver-Pierce model is consistent with that model, while the $I(\phi)$ function itself is quite different. This is a well-known mathematical difficulty with solving an "inverse problem."

C. Method III

A third method for determining $I(\phi)$ has recently been developed at Saclay. Figure 14 shows a toroidal topology containing a single weak link. If this device is rotated, at angular velocity $\mathbf{\Omega}$, about an axis normal to the plane of the loop, the superfluid well away from the weak link is constrained to rotate almost like a solid body: $v_s = \Omega r$, where r is the distance from the rotation axis. If the phase can advance by only integral multiples of 2π for a closed path within the torus, then the phase difference across the weak link is seen to be

$$\phi = 2\pi n + 2\pi \frac{2\Omega \pi r^2}{\kappa_3} = 2\pi n + 2\pi \frac{2\mathbf{\Omega}\cdot\mathbf{A}}{\kappa_3}, \tag{35}$$

where n is an integer and $\mathbf{A}$ is an area vector normal to the plane of the torus. Here for generality we have let $\mathbf{\Omega}$ and $\mathbf{A}$ point in arbitrary directions. The integer n can be nonzero if quantized vortices are trapped within the torus or if persistent currents exist around the torus. For a loop of sufficiently large area (several cm^2), reorientation of the loop with respect to the earth's rotation vector $\mathbf{\Omega}_E$ can vary ϕ continuously over a range larger than 2π. This gives the experimenter independent control of ϕ.

This phase variation method is utilized to measure the low-amplitude resonant frequency of a membrane-aperture superfluid oscillator when a parallel tube of length l and cross-sectional area a is connected in parallel with a slitlike weak link (Avenel *et al.*, 2000). The topology of this experiment is the same as in method I, but the slit is now etched in a silicon nitride membrane rather than the nickel foil used in earlier Saclay experiments. The inductance L of the parallel combination is given by

$$L = \frac{L_s L_w}{L_s + L_w}, \tag{36}$$

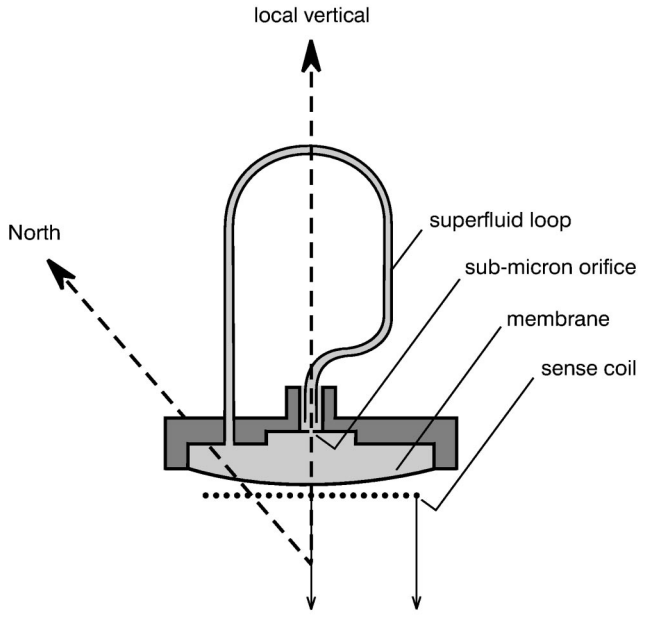

FIG. 14. The topology of a cell used for method III (Saclay). A weak link is shunted by a long parallel tube. The closed path enclosing the weak link and the tube has sufficient area that reorientation of the cell in the earth's rotational field creates phase differences given by Eq. (35).

where L_s is the hydrodynamic inductance of the parallel path [see Eq. (A2)] given by

$$L_s = \frac{l}{a\rho_s}, \tag{37}$$

and L_w is the weak-link inductance defined by Eq. (32).

For a nonlinear current-phase relationship $I(\phi)$, the inductance L_w is a function of the phase difference ϕ. The idea behind method III is to vary ϕ and thus L_w by reorienting the torus with respect to $\mathbf{\Omega}_E$ in order to phase-bias the weak link. The connection between phase bias and rotation is discussed further in Sec. XIV below.

Since the resonant frequency ω of the membrane-aperture oscillator is inversely proportional to $\sqrt{L}$, the frequency will change as L changes due to the changes of ϕ. This permits the experimentalist to sample the slope $dI/d\phi$ as a function of ϕ. It can be shown that, for the weak link (Avenel *et al.*, 2000),

$$\frac{dI}{d\phi} = \left(\frac{\omega^2}{\omega_L^2} - 1\right)\frac{\kappa_3}{2\pi L_s}. \tag{38}$$

Here ω_L is the observed frequency when the oscillator is driven at such high current that negligible mass is assumed to flow through the weak link. Thus, by measuring the small-amplitude resonant frequency ω as a function of the orientation of the cryostat and assuming the phase is given by Eq. (35), one can determine the local slope $dI/d\phi$ as a function of ϕ and upon integration determine $I(\phi)$.

The Saclay group reports that $I(\phi)$ for the slit studied using this technique is history dependent. That is, for a given temperature, four different $I(\phi)$ functions were observed in four different cooldowns. The well-defined family of curves observed in nanoaperture arrays does not seem to be present in this slit. However, at approximately zero ambient pressure the general shape of the data [Fig. 15(b)] resembles that found in Fig. 13. Since the earlier Saclay work using method I suggested a distinctly different $I(\phi)$ (Fig. 11), one might conclude that the silicon nitride slit has a different $I(\phi)$ from the nickel slit or that method I did not reveal the correct $I(\phi)$ function, because the Deaver-Pierce parametrization is mathematically incapable of representing $I(\phi)$ functions of the form measured directly by methods II and III (as shown in Figs. 13 and 15).

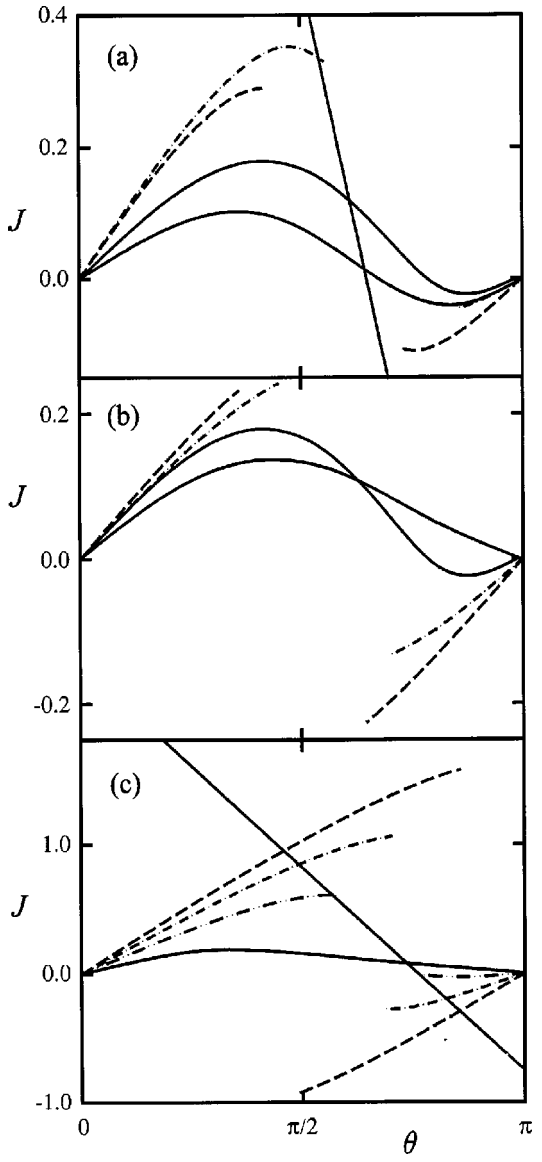

FIG. 15. Current-phase relations deduced by using method III for a slit weak link: (a) Four $I(\phi)$ curves made at the same temperature but in different cooldowns. Mathematically, none of these curves can be described by the Deaver-Pierce parametrization (Fig. 9). (b) $I(\phi)$ curves from the same cooldown but at four different temperatures. The lowest maximum current curve is sinelike, whereas the larger current curves, which presumably are at a lower temperature, display positive slope at $\phi = \pi$.

IX. UNEXPECTED NEW PHYSICS IN $I(\phi)$

For conventional *s*-wave superconductors, the wave function is a complex scalar, and the only degree of freedom that can modify a sinelike $I(\phi)$ is a series inductance. This leads to the Deaver-Pierce parametrization. By contrast, ^{3}He is described by a tensorlike wave function, which can lead to greater complexity (Vollhardt and Wölfe, 1990). It is not surprising, therefore, that the ^{3}He weak-link current-phase relation exhibits phenomena not seen in conventional superconductors.

A. Bistability in ξ-sized apertures

Direct measurement of $I(\phi)$ (using method II) for the nanoaperture array led to the unexpected discovery of two families of $I(\phi)$ functions (Marchenkov *et al.*, 1999) as shown in Fig. 13. When the liquid is cooled through the superfluid transition, the weak-link properties appear to be set by freezing in some internal degree of freedom. This results in two (and only two) families of temperature-dependent $I(\phi)$ curves. Apparently, the internal configuration of the weak link and its associated set of $I(\phi)$'s can only be changed by going above T_c and then cooling back down.

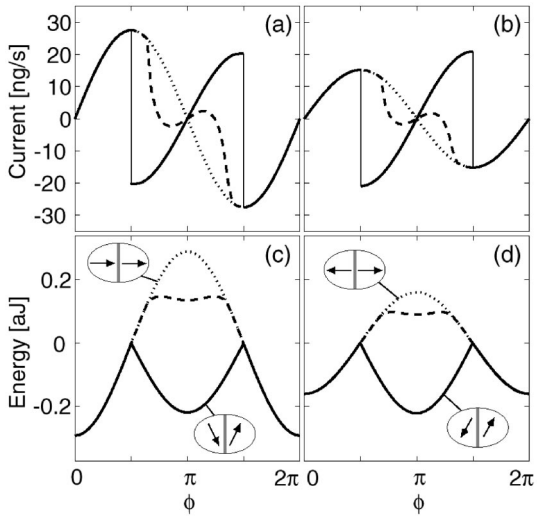

FIG. 16. A model for the source of bistability in the ^{3}He weak link. Parts (a) and (b) show calculated $I(\phi)$ for three different values of Ginzburg-Landau parameters in the model. For some values of the parameter describing the textural bending energy, the **n** vectors will switch from a uniform to a nonuniform texture at a well-defined phase difference. (a) $I(\phi)$ functions when the **n** vectors are parallel for $\phi=0$; (b) $I(\phi)$ functions when the **n** vectors are antiparallel for $\phi=0$; (c),(d) the calculated weak-link energies as a function of phase for these two cases (Viljas and Thuneberg, 1999).

The two families of $I(\phi)$ are shown in Fig. 13. Both families show the same generic character: sinelike at high temperatures and acquiring a strong $\sin(2\phi)$ component at lower temperatures. At a given temperature, the curves differ in maximum currents and are labeled H and L for high and low current, respectively. The critical current [defined as the maximum of $I(\phi)$] of the H state is given by $1.3\times10^{-10}\,(1-T/T_c)^{1.5}$ kg/s, while for the L state it is $6.8\times10^{-11}\,(1-T/T_c)^2$ kg/s.

Although it was expected that only one $I(\phi)$ would characterize a ^{3}He weak link, more recent theories (Viljas and Thuneberg, 1999, 2002; Yip, 1999) show different ways that two families of $I(\phi)$ relations can arise from different orientations of the internal vector field **n** (which characterizes bulk ^{3}He-B).

Using a Ginzburg-Landau formalism, Thuneberg and Viljas derive the $I(\phi)$ functions resulting from **n**'s being both parallel and antiparallel to the normal to the plane containing the weak link. The model's central predictions are shown schematically in Fig. 16. There is a close similarity between these model results and the families of current-phase curves in Fig. 13. To find agreement both in form and magnitude, three model parameters need to be adjusted to values within an order of magnitude of those directly predicted in the theory.

In other work using a Green's-function approach, Yip (1999) also finds the possibility of two families of $I(\phi)$ functions. For this model, in the absence of magnetic fields, when the **n** vectors are parallel on both sides of the weak link, the current-phase relation has no $\sin(2\phi)$ component at any temperature. In contrast, when the **n**'s are antiparallel, there is always a $\sin(2\phi)$ component at all temperatures.

B. Weak links displaying a variety of $I(\phi)$'s

The theories of Viljas and Thuneberg, and of Yip, which show the important role of the **n** field in determining $I(\phi)$, may also offer an explanation of why the slit aperture used in method III shows a multiplicity of current-phase relations, whereas the ξ-sized apertures in the Berkeley nanoaperture array reveal only the two $I(\phi)$'s found in the theory of Viljas and Thuneberg (1999). Perhaps the slit, which has a length much longer than ξ, simply permits a variety of metastable **n** textures pinned to rough spots along the walls. Each texture might give rise to a different $I(\phi)$.

To test these new theories, one needs to measure $I(\phi)$ while controlling the orientation of a magnetic field relative to the normal of the junction and in a geometry where the **n** texture is understood. The coupling between **n** and the field should reveal more clearly the effect of the texture on $I(\phi)$. Preliminary results from such experiments are now becoming available (Mukharsky *et al.*, 2001). A single slitlike aperture was studied and many different $I(\phi)$ states were detected (on different cooldowns). Each $I(\phi)$ could be continuously changed by varying the magnetic field. These data support the idea that the different $I(\phi)$'s are the result of different textures and that, in a large slit, these textures can be varied quite significantly.

Although it is too soon to be sure, one may speculate that an array of ξ-sized apertures can somehow lock the overall weak link into the lowest available energy states of the texture, most likely the "isotextural" (Viljas and Thuneberg, 2002) case.

C. π states

A second unexpected discovery involved a metastable state with π phase bias across the weak-link array. The observed phenomena can be understood in terms of the energy stored in the phase shift across the weak link. The mechanical power applied to the system is the product PI/ρ. This is the analog of the product of current and voltage for an electrical device. The energy stored in the weak link is given by

$$E=\int_0^t \frac{PI}{\rho}\,dt. \tag{39}$$

By combining Eqs. (8) and (20), one sees that

$$\frac{P}{\rho}=\frac{\kappa_3}{2\pi}\frac{d\phi}{dt}. \tag{40}$$

Combining Eqs. (39) and (40) gives

$$E=\frac{\kappa_3}{2\pi}\int_0^{\phi} I(\phi')\,d\phi'. \tag{41}$$

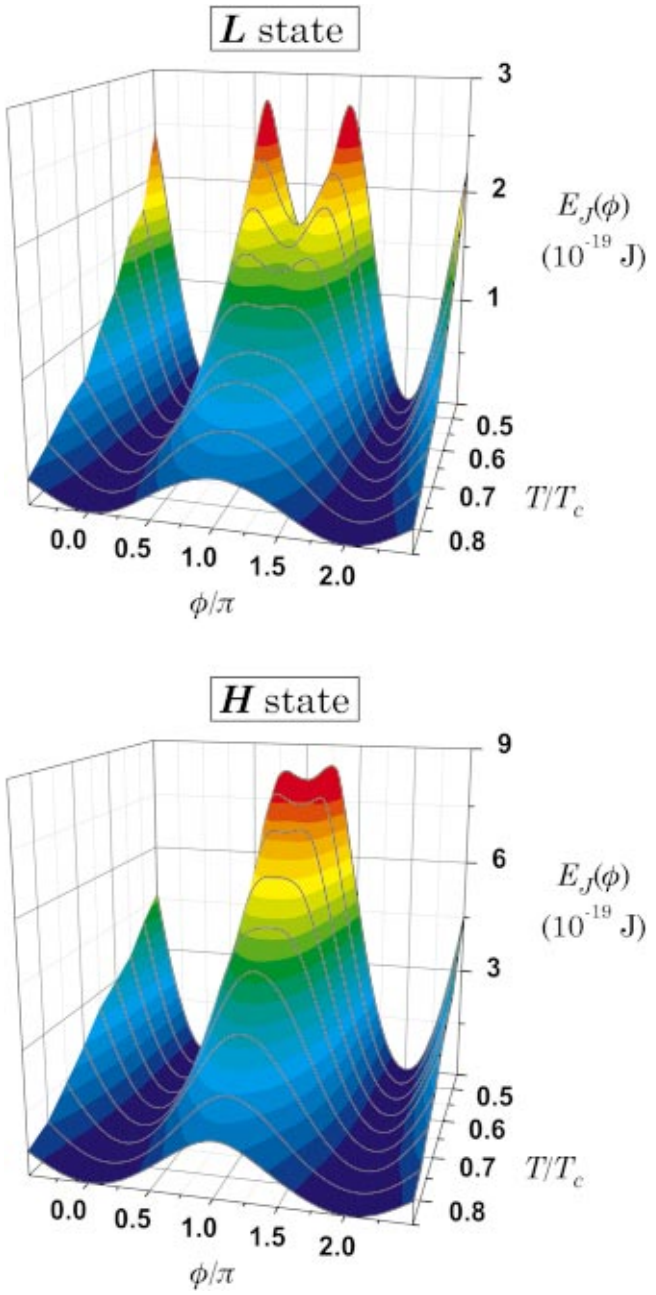

FIG. 17. The family of weak-link energy-phase curves deduced using Eq. (41) applied to the two sets of measured $I(\phi)$ functions shown in Fig. 13 [Color].

Thus, by integrating the current-phase relation, one obtains the weak-link energy as a function of phase difference. By integrating the curves shown in Fig. 13, one obtains the energy surfaces for the H and L states (Marchenkov *et al.*, 1999). These are shown in Fig. 17.

It is apparent that at temperatures where $I(\phi)$ has a positive slope at π, a local minimum appears in the energy. The depth of this potential well increases as temperature decreases. It is therefore possible that at a given temperature, the weak link might become metastably trapped with a π phase difference across it.

Such a phenomenon was discovered (Backhaus *et al.*, 1998) using a nanoaperture array, before the complex nature of $I(\phi)$ had been directly determined. As mentioned above, the nanoaperture array coupled to the membrane exhibits an oscillatory pendulum mode. If this mode is excited by a few resonant oscillations to a given amplitude of membrane motion, the decay of the oscillation can then be observed. When this experiment is performed at quite low temperatures ($T<0.4$ mK) and at sequentially higher excitations, the decay is observed until a critical amplitude of excitation is reached. For drives above this critical level, the oscillation seems to collapse, but after an arbitrary period of time (which can last many seconds), the energy spontaneously reappears. This remarkable behavior is shown in Fig. 18. In the lowest trace the oscillation increases for a few cycles (as a result of the applied resonant drive), and then the amplitude abruptly drops to a much lower level with a different frequency. Subsequently the system oscillates in that low-amplitude state for many cycles before abruptly jumping back to the original amplitude. It seems as if kinetic energy abruptly leaves the system for a long period, only to be reinserted later.

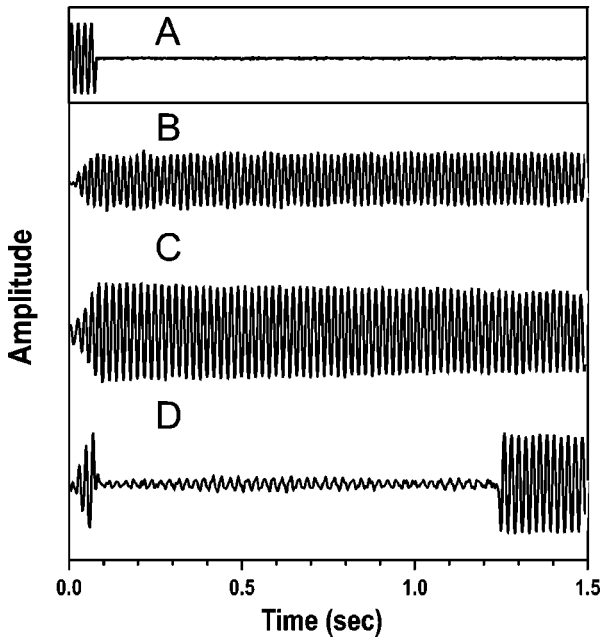

FIG. 18. Oscillation of the membrane resulting from the application of four cycles of drive at the pendulum mode resonant frequency at $0.3T/T_c$: Trace A is the wave form of the excitation. Traces B and C are the responses to successively increased drive amplitudes displaying characteristics similar to those of a high-Q pendulum. The amplitude of motion increases while the drive is applied. After the drive is turned off, the oscillations decay slowly due to the dissipation associated with the membrane motion. Trace D shows the departure from the behavior of a simple oscillator. The drive level has been adjusted so that the oscillator makes the transition to a new state near the time when the drive is turned off. Without further excitation, the oscillator "rings" freely in its new state until a random external perturbation causes a transition back to the original state. When the oscillator returns to its initial state, it regains the energy it had before the collapse. From Backhaus *et al.*, 1997.

The dynamics of the motion can be analyzed by plotting $d\phi/dt$ vs $\phi(t)$. Both of these quantities are ob-

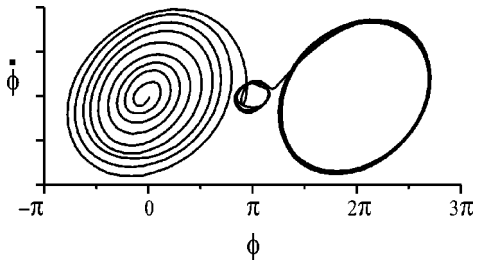

FIG. 19. A phase portrait of the motion before, during, and after a collapse. ϕ and $\dot{\phi}$ are determined from Eq. (30). During the excitation, consisting of eight cycles, the system orbits about the $\phi=0$ stability point, whereas after the collapse it orbits the $\phi=\pi$ metastable point. When the system makes the transition out of the π state, the system is then found to orbit either $\phi=0$ or $\phi=2\pi$.

tained from Eq. (30), which gives $\phi(t)$ in terms of the SQUID voltage. The resulting phase portrait of the motion is shown in Fig. 19. Here we see that during the excitation process the oscillator orbits a stability point around $\phi=0$. However, when the oscillation collapses, the system begins to make orbits of smaller amplitude around $\phi=\pi$. The oscillation at this new frequency can decay to zero, and the system is then trapped with a π phase difference across the junction. This is referred to as the *π state*, and by contrast, oscillations about $\phi=0$ are referred to as the *0 state*. When the oscillation abruptly reappears, the system again orbits around 2π or 0. The survival time, which is not under the control of the observer, grows longer as temperature decreases reaching as long as 1 h at temperatures below $0.25T_c$.

This behavior is completely consistent with the energy surfaces shown in Fig. 17. The absolute local minimum in $E(\phi)$, which occurs at $\phi=2\pi n$ (where n is an integer), leads to periodic motion characteristic of the rigid pendulum described in Sec. VI. This is the 0 state. If the temperature is sufficiently low and the drive amplitude sufficiently large, it is possible for the system to evolve into the local minimum at π. Dissipation or external mechanical noise can then allow the weak link to become trapped in the π state. The different frequency of oscillations for π states relative to 0 states is due to the difference in curvatures of $E(\phi)$ near $\phi=0$ and $\phi=\pi$. Both the H family and the L family of $I(\phi)$ show π states, and their frequencies are in excellent agreement with those predicted for the appropriate $E(\phi)$.

There have been several different explanations advanced for the origin of the π state.

(1) Since positive slope of $I(\phi)$ at π is the requirement for a local energy minimum there, π states are implicitly predicted by the work of both Viljas and Thuneberg (1999, 2002) and Yip (1999).
(2) An alternative approach was developed by Smerzi *et al.* (2001) and also by Hatakenaka (1998). These authors considered the behavior of weakly coupled quantum systems such as Bose-Einstein condensates. Using Feynman's treatment of the weak link with an added constraint of fixed particle number, they found an effective $I(\phi)$ that would exhibit a π state. To test these fascinating ideas, one would presumably need a condensate with much smaller particle numbers than the typical ^{3}He system.
(3) A third model for the π state was suggested by the Saclay group based on their Deaver-Pierce model of a weak link (Avenel *et al.*, 1999). If the Deaver-Pierce model were correct, for phase differences near π and $\alpha>1$, there is a double-valued current-phase relation with branches labeled I_+ and I_-. Avenel *et al.* point out that, in a nanoaperture array, if the $I(\phi)$ of each nanoaperture can be parametrized by the Deaver-Pierce model, and if approximately half of the apertures reside on the I_+ branch and half on the I_- branch, the effective $I(\phi)$ of the array would have positive slope at π and therefore would lead to a metastable state whose stability point is near $\phi=\pi$. This model predicts that the effective $I(\phi)$ function for the aperture array is discontinuous, which, as seen in Fig. 13, is not in agreement with the observations. Furthermore, these authors subsequently remeasured the current-phase relation of a single-slit aperture, using method III described above. They reported a single-valued $I(\phi)$ with positive slope near π, demonstrating that the π state is an intrinsic property of an individual aperture (Avenel *et al.*, 2000).

X. PENDULUM MODE

In Sec. VI we described how the membrane's equation of motion (which describes a coupled Josephson weak link and membrane) predicts that the membrane displacement mimics the angular velocity of a rigid pendulum. As shown schematically in Fig. 5(a), for small-amplitude oscillations about equilibrium, the simple pendulum frequency ω_p is given by Eq. (25), whereas for large-amplitude oscillations about equilibrium, the frequency is amplitude dependent and should approach 0 as ϕ approaches π (Monien and Tewordt, 1987).

These features can be tested by studying transient responses such as those shown in Fig. 12. After a large excitation, Josephson oscillations accompany the positive pressure head across the weak link. When the time-average pressure relaxes to zero, oscillations about equilibrium begin. For these oscillations about $P=0$, it is clear that the frequency is amplitude dependent, rising as the amplitude falls. Figure 20 shows a plot of this frequency versus the phase oscillation amplitude. The quantum phase is measured by integrating the displacement transducer signal as described by Eq. (30). The frequency here is defined as the reciprocal of the period of motion. To compare to the data the figure also includes a plot of the calculated frequency as a function of ϕ for a rigid pendulum without damping. If the Q of the oscillator is large, one would expect the predictions for the frequency of the undamped pendulum to be a good representation of the phase oscillation frequency. The experiment demonstrates that the nanoaperture array, as

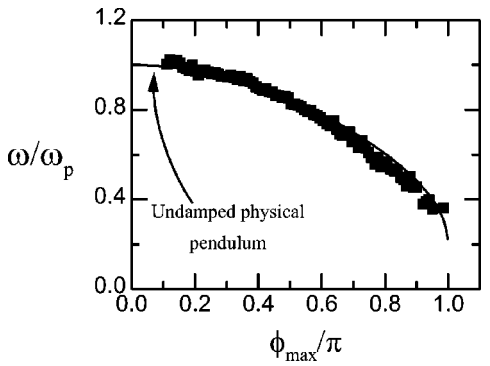

FIG. 20. A plot of the oscillator frequency as a function of maximum phase angle. An ideal rigid pendulum (without damping) would follow the smooth curve drawn as a solid line. The data are the average of approximately 50 transient ring-downs.

long as the temperature is sufficiently high ($T > 0.65T_c$), accurately displays the nonlinear rigid pendulum frequency.

Equation (25) predicts the dependence of small-amplitude oscillation frequency on the temperature-dependent critical current,

$$\omega_p^2 = \frac{2m_3\lambda}{A\rho^2\hbar} I_c , \tag{42}$$

where $\lambda = k/A$. Figure 21 shows the measured values of ω_p^2 as a function of I_c, the latter quantity being measured directly from $I(\phi)$ as described in method II. In the temperature region where $I(\phi)$ is sinelike there is excellent agreement with Eq. (42). When $I(\phi)$ is no longer sinelike the frequency is found to fall below the dashed line.

These experiments not only demonstrate again the sinelike nature of $I(\phi)$ for small apertures, but, perhaps more importantly, suggest a convenient method of determining I_c directly by simply measuring the frequency of the small-amplitude oscillations.

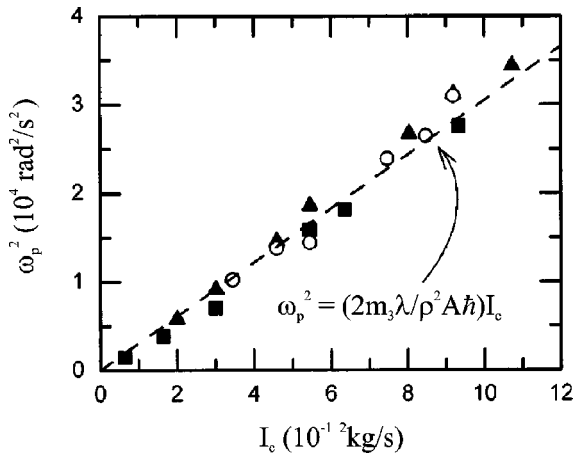

FIG. 21. A plot of the dependence of the pendulum (low-amplitude) frequency on the critical current. I_c was determined by measuring the complete current-phase relation in the temperature regime above $0.75T_c$, where $I(\phi)$ is sinelike. The straight line drawn is a plot of Eq. (42), which has no adjustable parameters. At lower temperatures, when $I(\phi)$ is no longer a simple sine function, the frequencies drop below the line.

XI. SHAPIRO EFFECT

For superconductors the first dynamic phenomenon involving both the Josephson current-phase relation [Eq. (5)] and the phase evolution equation [Eq. (8)] was the current "steps" observed by Shapiro (1963) when a microwave field impinged on a Josephson junction. The fact that an oscillating chemical-potential field mixes with the Josephson oscillations to produce a dc current is a consequence of the interplay between the two equations (5) and (8).

To observe similar effects in superfluid ^{3}He, one may apply an oscillating pressure field at frequency ω while the apertures are biased with a dc pressure $P_{\rm dc}$. When the Josephson frequency [Eq. (26)] is an integral multiple of the applied frequency [Eq. (11)], the theory predicts dc mass current steps I_n of magnitude

$$I_n = I_c \left| J_n\left(\frac{2m_3 P_{\rm ac}/\rho}{\hbar\omega}\right)\right| . \tag{43}$$

Here $P_{\rm ac}$ is the amplitude of the impressed pressure field and J_n is the nth-order cylindrical Bessel function.

Searches for Shapiro-like phenomena in ^{4}He by Anderson and Richards (1965) launched the entire field of superfluid weak links. Several other independent searches using ^{4}He were not conclusive (Tilley and Tilley, 1990), presumably because the apertures used were much larger than the coherence length. Early positive indications of an effect were later interpreted in terms of other acoustic phenomena not associated with weak-link behavior.

The first attempt to observe a ^{3}He Shapiro effect was reported by Lounasmaa *et al.* (1983) in Helsinki. Their weak link consisted of a random array of ~700-nm-diameter cylinders etched through a 6-μm-thick plastic membrane. The apparatus used membranes to drive and detect mass currents through these pores. The current-pressure (I-P) characteristic of these pores was measured in the presence of an ac applied pressure difference. They found that there were no Shapiro-like features for apertures with this aspect ratio. This was presumably because the apertures, which were many coherence lengths long, will not exhibit sin ϕ current-phase relations (Hook, 1987). However, for currents greater than some critical value, they did notice unexpected dissipative currents that, as described in Sec. XII, are now believed to occur due to superfluid velocity oscillations at the Josephson frequency.

Following the Helsinki results a search was made for Shapiro phenomena using a single aperture with this type of long aspect ratio (Pekola *et al.*, 1987). The idea was that perhaps incoherence between the millions of pores in the Helsinki experiment might have obscured the effect. Although again dissipation consistent with superfluid velocity oscillations was observed, no Shapiro signature was detected.

This situation changed with the discovery that nanoaperture arrays behave like Josephson weak links. In order to detect the Shapiro effect, the Berkeley double-diaphragm cell (shown schematically in Fig. 6) was reinstrumented with the capability of simultaneously applying both ac and dc pressure fields while monitoring the dc mass current through the nanoaperture array. This is accomplished by the configuration shown schematically in Fig. 6. The upper membrane serves as a dc pressure gauge (as described in Sec. V). The lower membrane is metalized and also has an adjacent electrode. A feedback loop is formed that applies voltages to the lower electrode set so that the dc deflection of the upper membrane is held fixed, thus maintaining a constant dc pressure head across the weak links (Backhaus and Packard, 1996).

An additional ac voltage is applied between the upper membrane and an adjacent electrode, creating an ac pressure field. Due to small effects of hydrodynamic inductance in series with the top membrane, the ac pressure $P_{\rm ac}$ across the weak link is not exactly equal to the pressure P_V delivered electrostatically to the top membrane. We define a frequency-dependent transfer function ν_n (of magnitude close to 1) such that $P_{\rm ac}/P_V \equiv \nu_n$ for each harmonic n of ω.

The mass current through the weak link is measured by monitoring the time evolution of the feedback voltage V. The mass current is given by

$$I = \frac{1}{2}\frac{\varepsilon\Lambda^2\rho}{d^2 k_l}\frac{d(V^2)}{dt}, \tag{44}$$

where ε is the liquid's permittivity, Λ is the effective area of the lower membrane, d is the effective gap between the electrodes, and k_l is the stiffness constant of the lower membrane.

In order to predict the form of the expected current features as a function of ω, one can perform a numerical simulation (Simmonds, Marchenkov, Davis, *et al.*, 2001) combining a $\sin\phi$ current-phase relation with a time-varying pressure field containing both dc and ac components. This differs from the standard superconducting case because it is equivalent to a voltage-biased weak link instead of the usual superconducting current-bias situation. In the simulation the time evolution of ϕ and I appears very complex, but a well-defined time-averaged, mass current can be determined. A typical result of such a simulation in the range where $\omega_J \sim \omega$ is shown in Fig. 22. As a practical definition of the current "step" $I_n^{\rm sim}$ in the simulations, one can take the peak-peak magnitude of the feature shown in the figure.

Using the apparatus shown in Fig. 6, one can clearly see current features at the frequency-matching conditions of Eq. (11), $\omega_J = n\omega$. A typical experimental signature is shown in Fig. 23. The close resemblance between this and Fig. 22 indicates that the predicted phenomena are occurring. The peak-peak magnitude of the experimentally observed feature, $I_n^{\rm exp}/I_c$, is plotted as a function of $(2m_3P_{\rm ac}/\rho)/\hbar\omega$ in Figs. 24(b) and 24(c) for $n = 1$ and 2. The Bessel function evolution clearly demonstrates the superfluid Shapiro effect for $n = 1$ and 2.

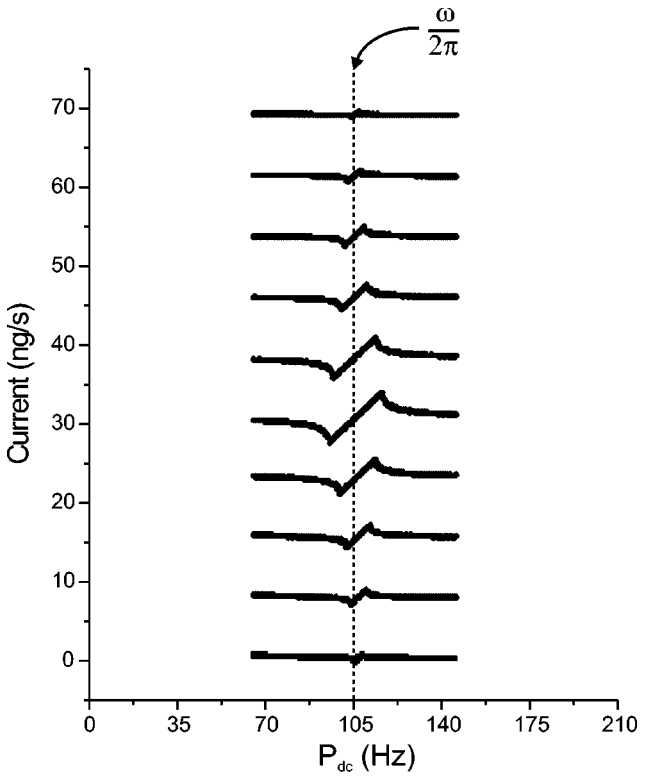

FIG. 22. A numerical simulation of the changes occurring in the dc mass current in a pressure range near $\omega_J \approx \omega_1$, for different values of the ac pressure amplitude. The horizontal axis represents dc pressure expressed in units of frequency $f \equiv 2m_3P_{\rm dc}/\rho h$. The vertical axis is the mass current. The *I-P* curves are shifted upward from each other by a constant amount for clarity. Each shifted plot represents an increase in the ac pressure amplitude. The vertical line identifies ω.

Probing the $n = 0$ Shapiro effect requires a different technique because the existence of currents at $\omega_J = 0$ (i.e., $P_{\rm dc} = 0$) requires current biasing. The effective critical current of the nanoaperture array is now I_0, as given by Eq. (43). Recalling that the pendulum mode frequency ω_p is a measure of the zero-pressure critical mass current according to Eq. (42), one can measure the $n = 0$ Shapiro effect by measuring ω_p as a function of $(2m_3P_{\rm ac}/\rho)/\hbar\omega$. Figure 24(a) plots the ratio $I_0/I_c \equiv \omega_p^2(P_{\rm ac})/\omega_p^2(P_{\rm ac}=0)$. Again, one sees excellent agreement between the predictions of Eq. (43) and the observations.

Even though earlier measurements established the $\sin\phi$ nature of the nanoaperture array weak links, it is nevertheless remarkable that no complications interfere at higher frequencies to destroy the interplay between Eqs. (5) and (8), whose solution leads to the Shapiro effect. Although the superfluid Shapiro effect was observed after the measurements of $I(\phi)$, its observation is nonetheless satisfying, since searches for it had been the driving force in the field for many years.

A related phenomenon occurs when the Josephson oscillations are resonant with some vibrational normal mode of the cell. This is analogous to the Fiske effect in superconducting weak links. A dc pressure applied

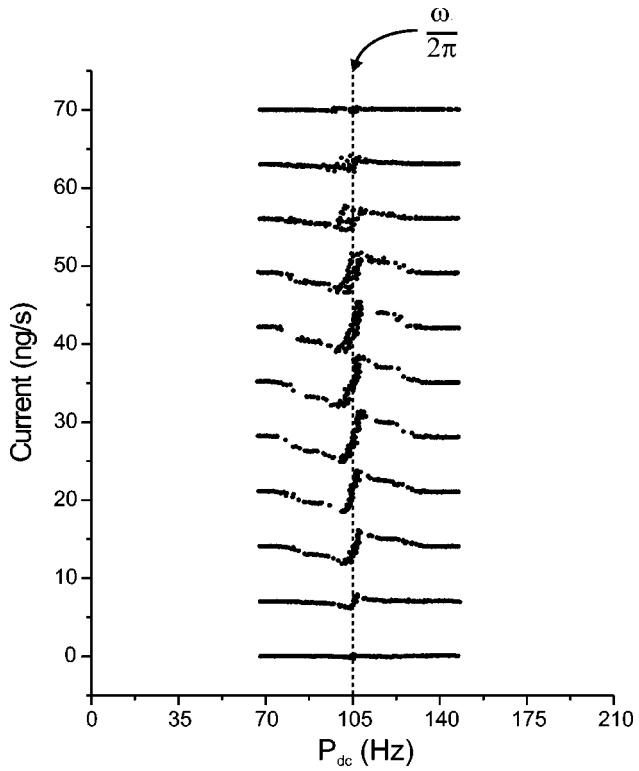

FIG. 23. A series of *I-P* curves measured in a pressure range near $\omega_J \approx \omega$ for different values of the ac pressure amplitude. The horizontal axis represents dc pressure expressed in units of frequency $f \equiv 2m_3 P_{\rm dc}/\rho h$. The vertical axis is the mass current. The *I-P* curves are shifted upward from each other by a constant amount for clarity. Each shifted plot represents an increase in the ac pressure amplitude. The vertical line identifies ω.

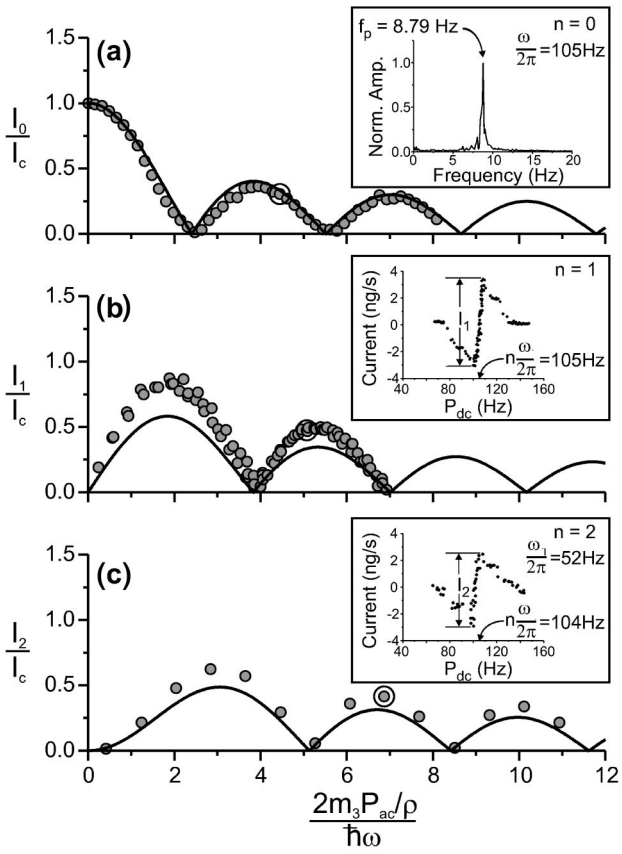

FIG. 24. The superfluid ^{3}He Shapiro effect: (a) The $n=0$ case. A plot of the ratio $I_0/I_c \equiv \omega_p^2(P_{\rm ac})/\omega_p^2(P_{\rm ac}=0)$ as a function of $(2m_3P_{\rm ac}/\rho)/\hbar\omega$. For $n=0$, the value of the transfer function $P_{\rm ac}/P_V \equiv \nu_0 = 1.25$ is determined by requiring the zeros of our data to fit the zeros of the Bessel function J_0. The solid line in this panel is the prediction for the zero-pressure mass current I_0/I_c. We determine the frequency ω_p by taking the Fourier transform of the low-amplitude segment of the pendulum-mode motion of the membrane. A typical Fourier transform of the pendulum mode is shown in the inset panel. (b) The $n=1$ case. A plot of the current feature I_1/I_c as a function of $(2m_3P_{\rm ac}/\rho)/\hbar\omega$. The inset shows that the current feature occurs at $\omega_J = \omega$ and indicates our definition of I_1. Fitting the data to the J_1 Bessel function zeros gives the value $\nu_1 = 1.16$. (c) The $n=2$ case, which is similar to (b), except now $\omega_j = 2\omega$. Here $\nu_2 = 1.04$. The data in each inset are associated with the circled data point in the associated panel.

across the weak link will create Josephson current oscillations at frequency ω_j. These oscillating currents in turn may excite a local resonance, which results in an additional (back-action) pressure oscillation across the weak link. The combined dc pressure plus back-action oscillating pressure at ω_j results in a dc current feature related to those discussed in the Shapiro effect.

An analysis of the effect due to the lowest-lying mode of the double-membrane cell shown in Fig. 6 predicts an excess dc current given by

$$\Delta I_{\rm dc} = \frac{1}{2}\frac{2m_3}{\hbar}\frac{k_2\zeta}{\rho^2 A_2^2}\frac{I_c^2 Q}{\omega_j^2}, \tag{45}$$

where Q is the quality factor of the mode, k_1 and k_2 are the effective spring constants, and A_1 and A_2 the effective areas of the top and bottom membranes, respectively. For this particular mode the parameter ζ is given by $\zeta = (k_2/A_2^2)/(k_1/A_1^2 + k_2/A_2^2)$. For other modes ζ will have a different form. For any given cell mode, $\Delta I_{\rm dc}$ on resonance depends on a geometric factor times $I_c^2 Q/\omega_j^2$.

In an experiment to look for this phenomenon, the dc mass current was measured as a function of the static applied pressure difference, $P \propto \omega_j$, across the weak link (Simmonds *et al.*, 1998). In the resulting *I-P* characteristic curve, one finds conspicuous current peaks at well-defined static pressures. The cell's normal-mode frequencies and Q's are determined independently by studying the response function relating the membrane motion to the frequency of a swept external drive. As one can see in Fig. 25, one finds that the current peaks in the *I-P* curve occur whenever ω_j matches a cell resonance frequency.

In Fig. 26, $\Delta I_{\rm dc}$ is plotted as a function of $I_c^2 Q/\omega^2$ for the lowest cell mode, which occurs in the range between 100 and 500 Hz (as temperature is varied). The value of I_c (at each temperature) is determined from current-phase measurements using method II above. The plotted points agree with Eq. (45) within experimental pre-

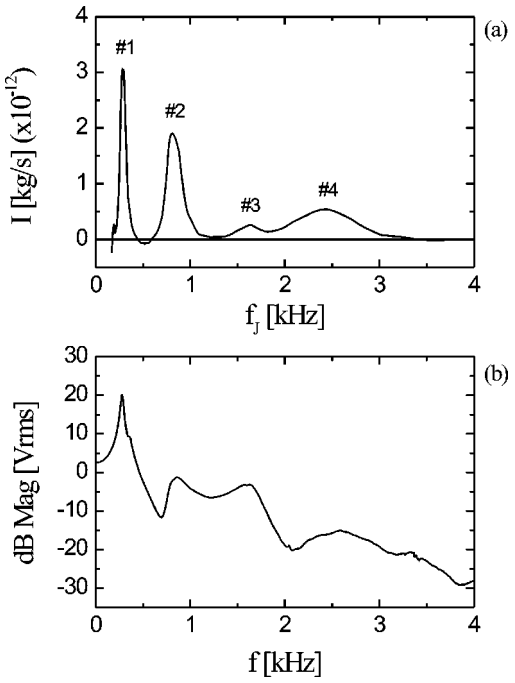

FIG. 25. The superfluid ^{3}He Fiske effect: (a) A typical current-pressure curve. A slowly varying background, associated with the dissipation mechanisms discussed in Sec. XII, has been removed to clarify the position of the peaks. This *I-P* curve was measured at $T/T_c=0.572$. (b) The response of the upper membrane when an oscillating force is applied to the lower membrane, also measured at $T/T_c=0.572$. The vertical scale is logarithmic.

cision until the temperature falls below the point where a simple sine function describes $I(\phi)$.

Both the Shapiro effect and the Fiske effect demonstrate that the ^{3}He weak link is well described by the finite-frequency phase dynamics resulting from Eqs. (5) and (8). Furthermore, the dc currents resulting from

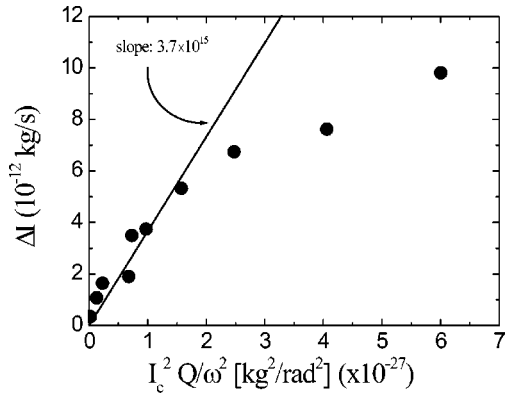

FIG. 26. Measured magnitude of the peak current enhancement, $\Delta I_{\rm dc}$, vs I_c^2Q/ω^2 for the lowest-frequency peak. For data with an abcissa value less than 2 [i.e., for which $T/T_c>0.64$, where $I(\phi)$ is known to be sinelike], the points fit a line that has a slope of $(3.7\pm0.3)\times10^{15}$ (SI). This agrees well with the prediction for a sinelike $I(\phi)$, which is shown as a solid line with slope 3.6×10^{15} (SI) from Eq. (45). At lower temperatures (on the right) the data depart from the prediction as expected.

these phenomena can serve as a convenient and sensitive measure of the critical current I_c. The need for such techniques becomes paramount in the use of a superfluid dc SQUID, discussed in Sec. XIV.

XII. INTRINSIC WEAK-LINK DISSIPATION

Although many of the phenomena described in the preceding sections agree exceedingly well with the predictions from Eqs. (5) and (8), the discoveries of bistability and π states were completely unexpected. Another unexpected feature is the large dissipation associated with Josephson oscillations. The very fact that the membrane relaxes to its mechanical equilibrium position after a large displacement (Fig. 12) implies that its potential energy has been dissipated by some mechanisms. Dissipative processes associated with the weak link are intrinsically interesting and, perhaps more importantly, will contribute to the thermal noise in any device based on these elements (e.g., a dc SQUID; Clarke, 1996).

There is one well-known dissipative effect that results from the conversion of superfluid to normal fluid during oscillatory superflow (Khalatnikov, 1965). This involves the so-called second-viscosity coefficient, which is relatively large for ^{3}He (Cook *et al.*, 1996). This damping mechanism correctly predicts the quality factors observed for pendulum motion about equilibrium (Simmonds, Marchenkov, Davis, *et al.*, 2000). However, in the regime of high-frequency Josephson oscillations, i.e., $P\neq0$, the second viscosity damping should be almost negligible.

The fact that a step increase in pressure differential relaxes to equilibrium in times typically less than a minute indicates that there is a large additional source of dissipation. This dissipation can be studied by determining the relationship between dc mass current through the weak link and the associated pressure head, i.e., the *I-P* characteristic, which is analogous to the *I-V* characteristic in a superconducting weak link. For a charged system, power dissipation $\dot{Q}$ equals IV. Similarly, for a neutral fluid, $\dot{Q}=IP/\rho$.

In order to determine the *I-P* characteristic, one may use the constant-pressure drive technique described in Sec. IX. The resultant families of temperature-dependent curves (one set for the H state and one set for the L state) are shown in Fig. 27. There are two remarkable features. The curves are not straight lines, clearly indicating the dissipation is non-Ohmic. Furthermore, for a given pressure P, the currents increase as temperature decreases, which implies that the dissipation gets greater as temperature is reduced, a nonintuitive result for superfluid.

Two dissipation processes can be identified, each describable as an independent conductance in parallel with the weak link, as shown in Fig. 28. One mechanism is equivalent to an Ohmic ($I\propto P$) conductance and the other is nonlinear such that $I\propto\sqrt{P}$. The curves in Fig. 27 can be well fit to a function of the form

$$I=I_1+I_2=G_1P+G_2\sqrt{P}, \tag{46}$$

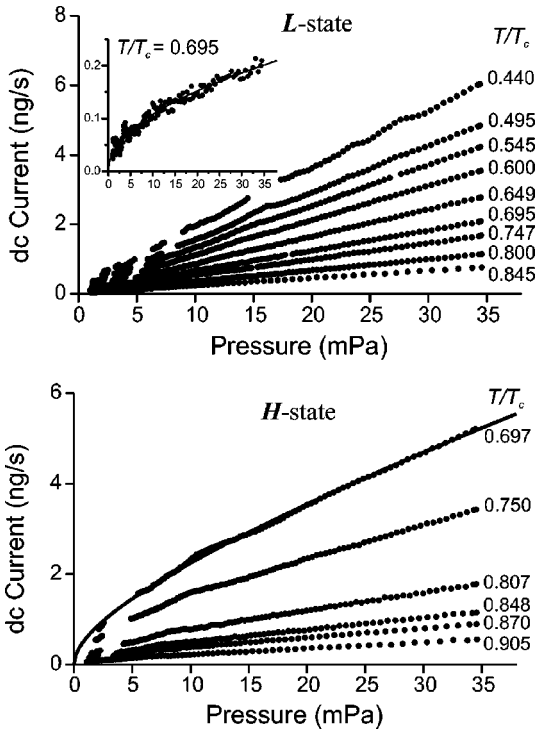

FIG. 27. The measured dc current is plotted as a function of the pressure across the weak link for both H and L states and critical currents below 25 ng/s. The gaps in the data are where the largest of the dc current enhancements (Fiske effect distortions) have been removed for clarity of fit. Some small distortions are still visible at low temperatures. For critical currents above ~25 ng/s, the I-P distortions become broad and are continuous throughout the accessible pressure range, making a meaningful fit to Eq. (46) problematic. The solid line (for $T/T_c=0.697$ in the H state) is an example of a fit to Eq. (46). The inset (for $T/T_c=0.695$ in the L state) shows the $\sqrt{P}$ character of the quasiparticle current I_2 (notice the small size of I_2 for the L state so that the I-P curves appear purely linear at first glance). To obtain this curve, a fit of the I-P curve was made to Eq. (46), producing G_1 and G_2. Then the quasiparticle current is given by $I-G_1P$ and the solid line is given by $I_2=G_2\sqrt{P}$.

where G_1 and G_2 are the linear and nonlinear conductance fit parameters, respectively.

The linear conductance G_1 can be qualitatively understood in terms of the so-called orbital viscosity (Wheatley, 1975; Cross, 1983) of superfluid ^{3}He. Although the bulk fluid surrounding the weak link (in the Berkeley experiments) is ^{3}He-B, when confined between solid walls separated by distances on the order of ξ, it is known from both theory (Fetter and Ullah, 1988; Li and Ho, 1988) and experiment (Freeman *et al.*, 1988) that the order parameter of the B phase must distort to that of an anisotropic superfluid similar to ^{3}He-A. An anisotropic superfluid is characterized by a unit vector field or $\hat{\boldsymbol{l}}$ texture, where $\hat{\boldsymbol{l}}$ points in the direction of the Cooper-pair angular momentum. When a chemical-potential difference exists between two points in the A phase, if the superfluid time-average acceleration is zero, $\hat{\boldsymbol{l}}$ will exhibit periodic motion at the Josephson frequency, as

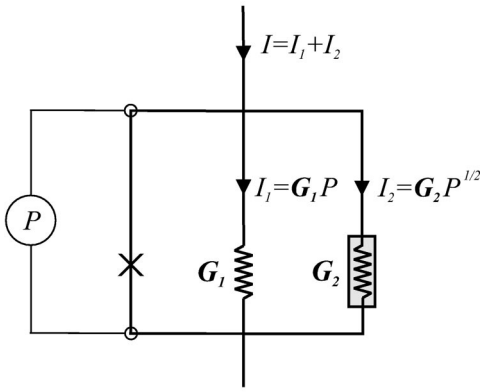

FIG. 28. Schematic of a weak link shunted by two dissipative elements G_1 and G_2.

shown schematically in Fig. 29(a). Thus the entire texture within the nanoaperture may be thought to precess at the Josephson frequency (Hall and Hook, 1977; Ho, 1978; Volovik, 1978).

Due to the finite relaxation time of quasiparticles, as shown schematically in Fig. 29(b), motion of the texture is an inherently dissipative process (Cross and Anderson, 1975; Cross, 1983) characterized by the orbital viscosity μ_l as the relevant dissipative coefficient. The power dissipated per unit volume is given by $\mu_l(d\hat{l}/dt)^2$.

The dc current associated with orbital precession may be estimated by equating the Ohmic power dissipation

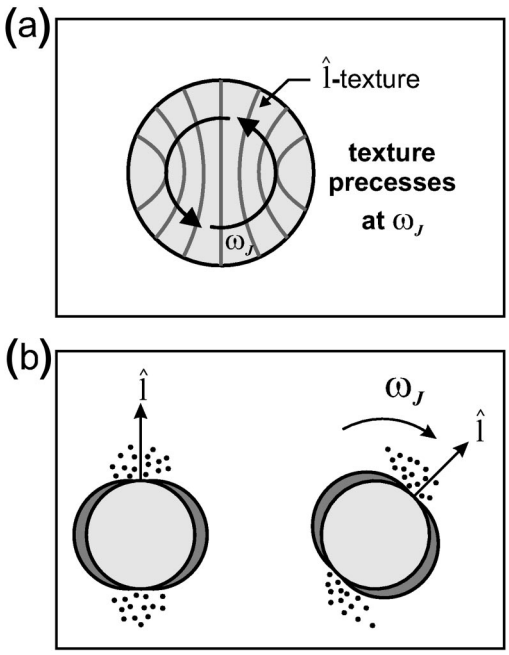

FIG. 29. A model for the component of weak-link dissipation which exhibits "Ohmic" conductance: (a) schematic of textural motions at the Josephson frequency in the aperture; (b) schematic of the physical source of Cross-Anderson orbital viscosity. The anisotropic superfluid energy gap surrounding the Fermi surface is shown falling to zero at the poles. The dots represent the distribution of quasiparticles, which must continuously relax towards the energy-gap nodes as it precesses at the Josephson frequency.

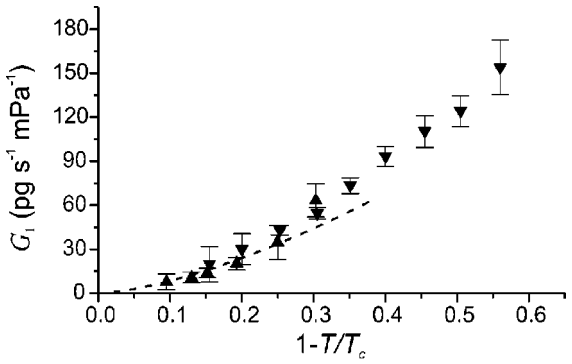

FIG. 30. The magnitude of G_1 plotted as a function of $(1-T/T_c)$ for ▲, the H state and ▼, the L state. The dashed line was generated using the theoretical expression for $\mu_l(T)$ (valid near T_c), with $\beta=1$ and the fit value $V_{\rm eff}=1.4\times10^{-21}$ m^3. The data agree very well with our prediction for *both* H and L states for temperatures near T_c.

to the time-averaged energy lost due to the precessing $\hat{l}$ vector:

$$\dot{Q}=\frac{IP}{\rho}=\left\langle \mu_l\int(\dot{\hat{\mathbf{l}}})^2d^3r\right\rangle\approx\beta\mu_l(\omega_J)^2\int d^3r$$
$$=\beta\mu_l\left(\frac{2m_3P}{\rho\hbar}\right)^2V_{\rm eff}. \quad (47)$$

Here the factor β, which is of order unity, represents an average over the spatial orientations of $(\hat{\mathbf{l}})^2$, and $V_{\rm eff}$ is the effective volume of the anisotropic phase region surrounding one aperture. Using the definition $I_1=G_1P$ and Eq. (47), we find that the conductance of N apertures is given by

$$G_1=\beta NV_{\rm eff}\frac{\mu_l}{\rho}\left(\frac{2m_3}{\hbar}\right)^2. \quad (48)$$

This expression is independent of the form of the current-phase relation of the weak-link array. The temperature dependence of G_1 comes mainly from the orbital viscosity coefficient because the effective volume of the A-phase region should not vary strongly with temperature (since the confining geometry alone stabilizes the state).

Fitting Eq. (46) to the data in Fig. 27 allows the extraction of G_1 as a function of temperature. Figure 30 is a plot of that G_1 vs T for both the H and the L states. The dotted line is the prediction of the theory calculated from Eq. (48) with $\beta=1$ and $V_{\rm eff}=1.4\times10^{-21}$ m^3, comparable to the volume of one aperture. As predicted by the model, due to the independence of this process from $I(\phi)$, the linear dissipation terms in both H and L states are the same. Furthermore, near T_c the data are quantitatively in agreement with the Ginzburg-Landau value of μ_1.

The nonlinear conductance G_2 originates in another mechanism (Marchenkov *et al.*, 1999) and can be described using a phenomenological model involving the concept of nonequilibrium creation of quasiparticles. Several intertwined phenomena lead to this dissipation:

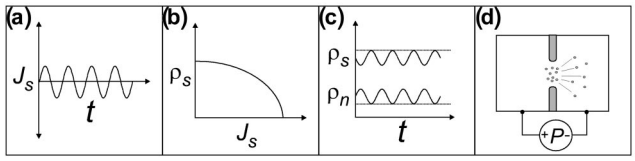

FIG. 31. Visualizing the creation of a quasiparticle current: (a) Josephson current oscillations in time; (b) the dependence of the superfluid density ρ_s as a function of the current density J_s; (c) the resultant *decremental* oscillations of ρ_s and the associated *incremental* oscillations in ρ_n; (d) ballistic quasiparticles being swept away from an aperture by the local pressure gradient.

(1) As described in Sec. VII.A, when a pressure head exists across the nanoaperture array, there is an associated mass current oscillating at the Josephson frequency.
(2) For a BCS-type superfluid ρ_s decreases with superfluid current density (Maki, 1978; Kleinert, 1980). Therefore the Josephson current oscillations will give rise to a *decremental* oscillation of ρ_s.
(3) The decrease in ρ_s is associated with the creation of quasiparticles within the aperture. It can be shown that these quasiparticles have initial group velocity very close to zero.
(4) Since, at millikelvin temperatures, the mean free path of the quasiparticles is very large compared to the dimensions of the aperture, they will be ballistically swept away from the apertures by the local pressure gradient.
(5) If the quasiparticles are propelled ballistically by the pressure gradient, they attain an average drift velocity $\langle v_n\rangle$ given from simple kinematics by $\langle v_n\rangle\approx\sqrt{2P/\rho}$. This is the proposed origin of the $\sqrt{P}$ dependence.

The elements of this model are shown schematically in Fig. 31.

The associated dissipative quasiparticle current density is $J_2\equiv\langle\delta\rho_n\rangle\langle v_n\rangle$, where $\langle\delta\rho_n\rangle$ is the time-averaged density of the quasiparticles created during a Josephson period. For N apertures with individual cross-sectional area σ, the total current is then proportional to $\sqrt{P}$ with proportionality constant

$$G_2\approx\langle\delta\rho_n\rangle N\sigma\sqrt{\frac{2}{\rho}}. \quad (49)$$

Since $\langle\delta\rho_n\rangle$ depends on the time variation of the supercurrent, the detailed shape of the current-phase relation $I(\phi)$ results in different values of G_2 for the H and L states. Using existing predictions for the suppression of the superfluid density with current density and knowledge of $I(\phi)$, one can generate the values for $\langle\delta\rho_n\rangle$ and from Eq. (49) predict G_2 as a function of temperature. The solid line in Fig. 32 shows the predictions for G_2 based on the $\rho_s(v_s)$ derived in a weak-coupling BCS treatment, valid for all temperatures (Kleinert, 1980). In

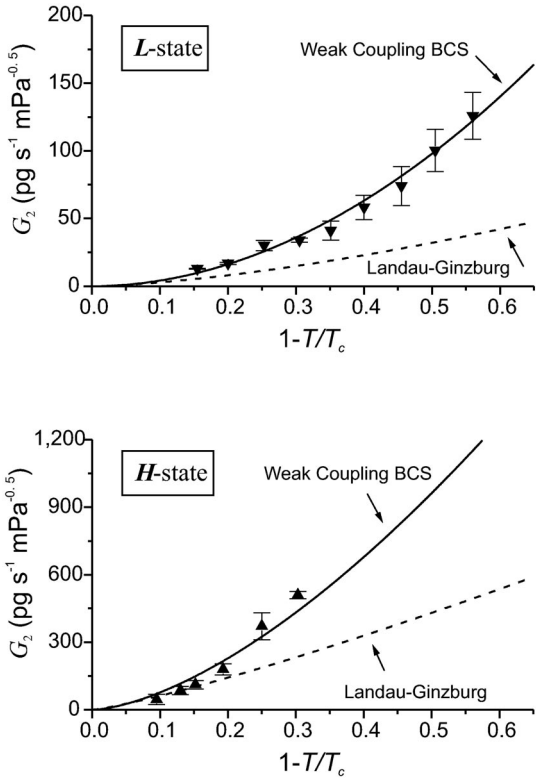

FIG. 32. The values for G_2 plotted as a function of $1-T/T_c$: ▲, for the H state; ▼, for the L state. The dashed line shows a prediction for G_2 using a Ginzburg-Landau model. The solid line shows a prediction for G_2 using a weak-coupling BCS treatment, valid for all temperatures.

the figure the measured values of G_2 for both states are also plotted. Notice the large difference between the values for G_2 in each state.

These curves are in good agreement with the data. In Eq. (49) the aperture area σ has been adjusted to get best agreement with *both* sets of data. This gives a *single* value, $\sigma=1.4\times10^{-21}$ m^2. Using effusion data, Marchenkov *et al.* (2002) independently found the aperture area to be $\sigma=1.36\times10^{-14}$ m.

No detailed theory has been developed to support these phenomenological models, and future work is required to provide a microscopic understanding of these phenomena.

The essential elements for explaining the nonlinear conductance are an oscillating mass current and a BCS velocity-induced density suppression. A pure Josephson oscillation is not necessary. Other ^{3}He mass flow experiments can include these elements. In particular, Lounasmaa *et al.* (1983) studied pressure-driven flow of superfluid ^{3}He through submicron pores whose length was too long to be a Josephson weak link. Nonetheless, they did observe nonlinear dissipation quite similar to that discussed above. There is no detectable dissipation until the current reaches a critical value I_c. Thereafter the time-averaged current can be described by

$$I\approx I_c+G_2\sqrt{P}. \tag{50}$$

Presumably, the instantaneous current resembles a sawtooth oscillation about I_c due to vortex-mediated phase slippage. The velocity amplitude of oscillations is approximately $\kappa_3/2L$, where L is the pore length.

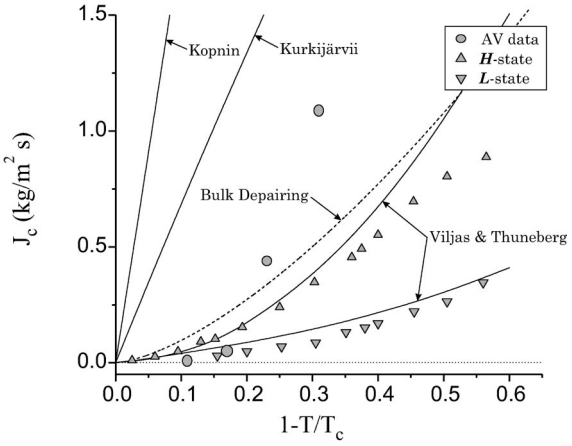

FIG. 33. Measured critical currents compared to various theoretical predictions. The Kopnin and Kurkijärvii models have very simple geometries and no adjustable parameters. The results from other theories are not plotted because no analytic expression for the critical current density as a function of temperature was reported. AV data are those of Avenel and Varoquaux, 1985.

The magnitude of G_2 in this case can be estimated by considering the BCS enhancement of $\langle\rho_n\rangle$ due to the sawtooth oscillations. Arguments similar to those above lead to an estimate of G_2 in agreement with the experiment. Thus the nonlinear dissipation observed by Lounasmaa *et al.* may have been an early indirect manifestation of superfluid oscillations occurring at the Josephson frequency, albeit without a sinelike $I(\phi)$.

XIII. CRITICAL CURRENTS

Microscopic theories of ^{3}He weak-link physics have attempted to compute the current-phase relation for various superfluid weak links with tractable geometries. These calculations, which are summarized in Sec. IV.C, yield functional forms $I(\phi)=I_0f(\phi)$, where $f(\phi)$ is some function spanning the range -1 to 1, which is 2π periodic in ϕ. Since the maximum current does not necessarily occur when $\phi=\pi$, we define I_0 as the maximum mass current possible at any phase difference.

There are two sets of experimental results for I_0 (Varoquaux *et al.*, 1992; Marchenkov *et al.*, 1999). To compare them, we divide the reported maximum mass currents I_0 by the nominal open area of the slit/array to yield the maximum mass current density J_c for each weak link as a function of temperature. In Fig. 33 we show the J_c data sets along with the predictions of Kopnin (1986), Kurkijärvii (1988), and recent calculations specifically for the nanoaperture array (Viljas and Thuneberg, 2002). We also show the bulk depairing mass current density at zero pressure.

The pinhole calculations of Kopnin and Kurkijärvii both overestimate the size of J_c as determined in the

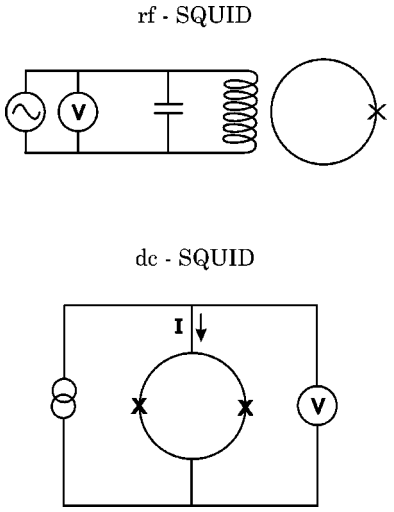

FIG. 34. Schematic differences between operational modes of an rf SQUID and a dc SQUID.

nanoaperture array, but are nearer to that of the slit (Varoquaux *et al.*, 1992), whose J_c rises very rapidly, crossing the depairing line near $0.8T/T_c$. The calculations of Viljas and Thuneberg, which use an "isotextural" model near the nanoaperture array, are in quite good agreement with the H and L states of the array. Similarly detailed calculations are not available for the geometry of the slit used at Saclay. Since the data are still quite limited, it is too soon to determine whether a predictive general model exists for the magnitude of the Josephson mass currents as a function of temperature, field, and geometry in ^{3}He weak links.

XIV. DC SQUID

A. Superfluid dc SQUID

The most important application of superconducting weak links are as detectors of magnetic flux, in devices referred to as superconducting quantum interference devices or SQUID's. These devices are generally classified as "rf" or "dc" SQUID's (Van Duzer and Turner, 1981; Barone and Paternò, 1982; Likharev, 1986; Tilley and Tilley, 1990). This historical nomenclature can be confusing. The rf SQUID *does not* involve quantum interference and does not necessarily have to be operated at radio frequencies. The dc SQUID *does* involve quantum interference but operates with biased Josephson weak links oscillating at gigahertz frequencies. Nevertheless, these designations persist. Figure 34(a) shows an rf SQUID, which is characterized by a close loop containing a single weak link (not necessarily sinelike). Figure 34(b) shows a dc SQUID, which contains a closed loop containing two weak links. Both of these devices rely on three facts: (1) The weak links must have a well-defined maximum supercurrent, e.g., a phase-slip onset current or the maximum of $I(\phi)$. (2) There is a macroscopic quantum phase which is coherent throughout the system. (3) There is a topologic constraint on the phase winding due to the loop geometry. These three features will result in physically measurable changes in the response of the loop when phase changes are created by external magnetic fields.

In the case of ^{4}He, only analogs of the rf SQUID have been demonstrated. Here $I(\phi)$ is linear but there is a maximum current determined by the phase-slip critical velocity (Avenel and Varoquaux, 1985; Varoquaux *et al.*, 1986; Beecken and Zimmermann, 1987a, 1987b; Davis *et al.*, 1992; Ihas *et al.*, 1992; Bonaldi *et al.*, 1994; Steinhauer *et al.*, 1995). Figure 14 shows a schematic diagram of the arrangement used at Saclay (Avenel *et al.*, 1997). The loop containing a small aperture is coupled to a flexible membrane; the entire assembly is a superfluid hydrodynamic oscillator. The plot of oscillation amplitude vs drive force shows a characteristic staircase pattern (Avenel and Varoquaux, 1985). The first plateau occurs when the drive force produces superflow in the aperture sufficient to generate 2π dissipative phase slips in each half cycle of motion due to the generation of quantized vortices. If the torus is rotating about an axis perpendicular to the plane of the loop, there is an additional current within the aperture as required by circulation quantization. Since the phase-slip critical current is intrinsic to the aperture, this additional current causes an apparent change in the drive force needed to create phase slippage. Therefore changes in rotation can be monitored by recording changes in the drive force necessary to create 2π phase slips (Schwab *et al.*, 1997). Even without a well-defined staircase, the state of rotation can be determined by monitoring each individual phase slip occurring in the oscillator (Avenel *et al.*, 1997).

In ^{3}He sinelike Josephson weak links exist, and both rf and dc SQUID analogs have been demonstrated. The rf device uses the same arrangement as in Fig. 14, except that the aperture is now of coherence length dimensions. This arrangement is topologically equivalent to the method I device used by Avenel and Varoquaux in $I(\phi)$ determination, shown in Fig. 8. The rf SQUID-like response pattern (shown schematically in Fig. 9) would presumably have changed if the device had been rotated. However, at that time a rotational degree of freedom was not a characteristic of the cryostat.

The more recent apparatus to determine $I(\phi)$ using method III is a different type of rf SQUID analog. As discussed in Sec. VIII.C, the method for determining $I(\phi)$ involved changes in kinetic inductance of the torus due to reorientation of the loop in the earth's rotational field. The reorientation changes the phase across a weak link. The line integral of the phase gradient around the loop must be an integral multiple of 2π. If the loop is rotated about an axis perpendicular to its plane, fluid flow similar to solid-body motion is induced in the fluid away from the weak link ($v_s \approx \Omega R$). In these regions the phase gradient is given by Eq. (17) as $\nabla\phi = (2m_3/\hbar)v_s$, and therefore

$$2\pi n = \oint \nabla\phi \cdot dl = \frac{2m_3}{\hbar}\int_a^b v_s \cdot dl + \phi = \frac{2m_3}{\hbar} 2\pi R^2 \Omega + \phi = \frac{2\pi}{\kappa_3} 2A\Omega + \phi, \tag{51}$$

where ϕ is the phase drop across the weak link and n is an integer. For $n=0$, the phase difference is thus proportional to rotation Ω. If the rotation vector $\mathbf{\Omega}$ is at an arbitrary orientation with respect to the normal area vector $\mathbf{A}$, then

$$\phi = -\frac{2\pi}{\kappa_3} 2\mathbf{\Omega}\cdot\mathbf{A}. \tag{52}$$

On the rotating earth, if A is greater than about 4 cm^2, reorientation of a cryostat with respect to the local vertical can modulate ϕ through at least 2π (Avenel *et al.*, 2000). Thus reorientation of the loop creates a controlled phase bias across the weak link. The system is a novel implementation of a single weak-link rf SQUID in which the effect of rotation on the kinetic inductance is detected through Eq. (32).

The phase shift given by Eq. (52) can be viewed as the superfluid version of the general "Sagnac" phase shift, $\Phi = 4\pi m\mathbf{A}\cdot\mathbf{\Omega}/h$ (where h is Planck's constant), which occurs in any rotating double-path quantum interferometer using particles of mass m. In the case of photons, one uses E/c^2 instead of m, where E is the photon energy and c the speed of light. This phenomenon is well studied for beams of photons (Stedman, 1997), neutrons (Werner *et al.*, 1979), and atoms (Keith *et al.*, 1991).

A double-junction superfluid dc SQUID has also been demonstrated (Simmonds, Marchenkov, Hoskinson, *et al.*, 2001). Figure 35(a) shows a schematic diagram of the device, consisting of a loop interrupted by two matched nanoaperture array weak links. The system rotates about an axis perpendicular to the loop. The total external mass current passing through the loop is given by

$$\begin{aligned} I_t &= I_c \sin\phi_1 + I_c \sin\phi_2 \\ &= 2I_c \cos\left(\frac{\phi_1-\phi_2}{2}\right)\sin\left(\frac{\phi_1+\phi_2}{2}\right), \end{aligned} \tag{53}$$

where I_c is the critical current of each weak link and ϕ_i is the phase difference across weak link i. The value of the argument of the cosine term can be obtained by considering the line integral of the phase gradient around the loop:

$$\begin{aligned} 2\pi n &= \oint \nabla\phi\cdot dl \\ &= \frac{2m_3}{\hbar}\int_a^b v_s\cdot dl + \phi_1 + \frac{2m_3}{\hbar}\int_c^d v_s\cdot dl - \phi_2 \\ &= \frac{2\pi}{\kappa_3}\mathbf{\Omega}\cdot\mathbf{A} + \phi_1 - \phi_2. \end{aligned} \tag{54}$$

With $n=0$, substituting $\phi_1-\phi_2$ from Eq. (54) into Eq. (53) yields

$$I_t = 2I_c \cos\left(\frac{\pi 2\mathbf{\Omega}\cdot\mathbf{A}}{\kappa_3}\right)\sin\left(\frac{\phi_1+\phi_2}{2}\right). \tag{55}$$

The argument of the sine function is the average phase difference across the input and output, $\Phi = (\phi_1-\phi_2)/2$. Thus Eq. (55) may be rewritten as

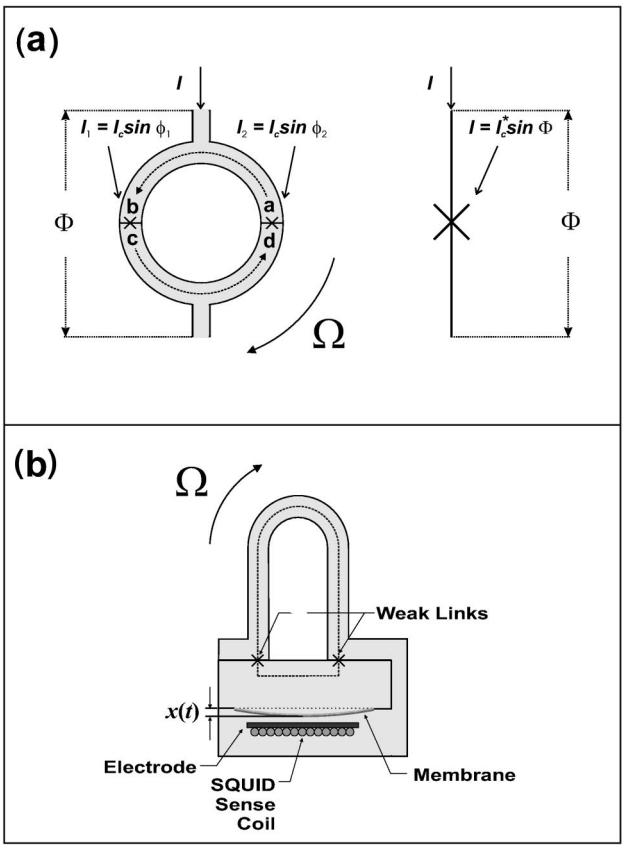

FIG. 35. The superfluid dc SQUID: (a) A schematic diagram of the basic superfluid dc SQUID interferometer loop; (b) the interferometer geometry used in the experiment. The nominal "loop" area is 6 cm^2 and the tube cross-sectional radius is 0.3 cm.

$$I_t = I_c^* \sin\Phi, \tag{56}$$

where we have defined an effective critical current

$$I_c^* \equiv 2I_c\left|\cos\frac{\pi 2\mathbf{\Omega}\cdot\mathbf{A}}{\kappa_3}\right|. \tag{57}$$

Thus the entire superfluid dc SQUID behaves as a single Josephson weak link whose maximum current may be modulated by rotation through Eq. (57).

An experimental test of these predictions has been performed using an apparatus shown schematically in Fig. 35(b) (Simmonds, Marchenkov, Hoskinson, *et al.*, 2001). The pressure- and current-sensing elements used technology similar to that described in Sec. V. There were two objectives of the experiment. The first was to determine whether the superfluid dc SQUID is describable by the current-phase relation given by Eq. (56). This would be demonstrated by the observation of phenomena such as Josephson oscillations or pendulum motion or direct measurement of $I(\phi)$ as described in Secs. VII, VIII, and X. The second objective was to determine whether the effective critical current can be modulated by reorienting the toroidal loop with respect to the earth's rotation vector according to Eq. (57).

The nominal loop area was 6 cm^2, chosen so that the earth's daily rotation would provide several cycles of modulation in I_c^* when the cryostat was reoriented by

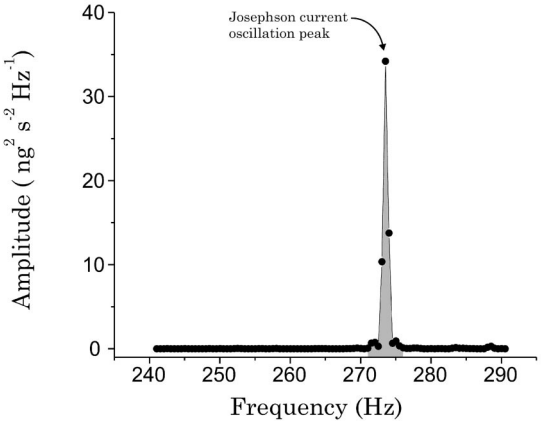

FIG. 36. The spectrum of the mass current during a 1-s interval of the data stream from the SQUID transducer. A typical data stream lasts 6 s, limited by the magnitude of the voltage applied to the diaphragm. Due to imperfect pressure regulation, the Josephson peak drifts slightly during the 6-s data stream. Therefore the transient is broken into 1-s intervals and a fast Fourier transform (FFT) routine is used to produce a figure like that shown for each interval. The peak is due to the Josephson oscillation at 273 Hz. Seventeen data streams are recorded, and an average value of all 6×17 of the peaks is computed and taken as the measure of I_c^*, the critical current of the interferometer.

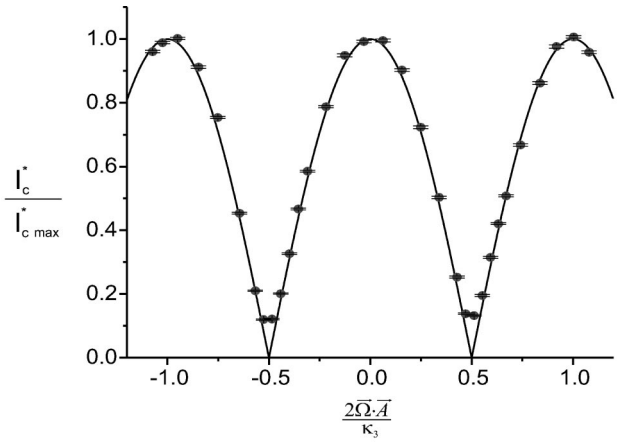

FIG. 37. A plot of the effective critical current I_c^* as a function of the rotation flux through the interferometer loop. The error bars, which are the standard deviation of 102 FFT's, are smaller than the size of the plotted points. The horizontal axis is normalized in units of the ^{3}He circulation quantum. The temperature was approximately $0.8T_c$. The rotation flux was varied by reorienting the normal to the loop's plane through an angle of $\pm\pi/2$ with respect to the east-west direction. The rotation flux is $\mathbf{\Omega}\cdot\mathbf{A}=\Omega_E A\cos\Theta_L\sin\theta$, where θ is the direction of $\mathbf{A}$ with respect to an east-west line and $\Theta_L\approx38°$ is the latitude of Berkeley. The solid line drawn is a plot of Eq. (57).

180° at the latitude of Berkeley, $\theta_L=38°$. The connecting tube had a nominal radius of 3 mm so that the kinetic inductance of the tube created negligible phase drop.

If the dc SQUID behaves as a single Josephson weak link, a static pressure differential applied across the interferometer should cause the quantum phase Φ to increase linearly in time [Eq. (8)], leading to mass current oscillations at the Josephson frequency.

As before, the deflection of the flexible membrane revealed both pressure across the interferometer and the mass current through it. A feedback method was used that permitted the system to be driven at constant pressure by applying a time-varying voltage to the membrane. A differential pressure was selected at which the Josephson frequency lay near 270 Hz, a spectral region away from parasitic acoustic noise lines in the displacement transducer, and also below the first acoustic standing-wave mode in the loop.

Figure 36 shows a Fourier transform of the mass current signal ($\propto\dot{x}$) through the interferometer resulting from the constant pressure differential applied for about 6 s. A sharp peak at 273 Hz is very pronounced. This corresponds to the Josephson oscillation. This frequency agrees with Eq. (28) to within the systematic uncertainty in the electrostatically derived pressure scale calibration. The oscillation frequency was found to scale linearly with P at least up to 1 kHz, and there were no higher harmonic signals within the signal-to-noise ratio of the experiment. This implies that the overall current-phase relation of the superfluid dc SQUID is sinelike and that the two separated arrays are phase coherent.

The magnitude of this Fourier peak is a direct measure of I_c^*. Therefore, if Eq. (57) is correct, reorientation of the cryostat will lead to a modulation of the peak amplitude. The amplitude of the Fourier peak is measured as a function of orientation angle θ of the cryostat. Since the applied rotation flux is not linear in θ, the observed modulation pattern is complex. For each angle θ, one can calculate that $2\mathbf{\Omega}\cdot\mathbf{A}=2\Omega_E A\cos\theta_L\sin\theta$ and then plot the Josephson peak as a function of $2\mathbf{\Omega}\cdot\mathbf{A}/\kappa_3$. Figure 37 shows such a plot. The cosinusoidal modulation predicted by Eq. (57) is displayed clearly. The scatter in the data is dominated by vibration noise associated with the building.

The interference pattern predicted by Eq. (57) and shown in Fig. 37 is the most striking feature of this experiment. The device displays a remarkable phenomenon: two-path quantum interference in a liquid. The pattern shows that the interferometer is a superfluid equivalent of a dc SQUID.

B. Noise considerations for a superfluid dc SQUID

It is natural to ask whether the superfluid quantum interference device could be developed into a sensitive rotation sensor, perhaps to perform meaningful geodesy measurements or experiments on general relativity. The earth's rotation vector is currently monitored with very-long-baseline interferometry (VLBI) techniques at a level of $10^{-10}\Omega_E$ in a one-day measuring time (Herring, 1991). A comparable level of gyroscopic sensitivity is required to observe the gravitomagnetic field of the earth as predicted by general relativity (Buchman *et al.*, 2000).

The minimal detectable change in rotation for a superfluid dc SQUID can be expressed as

$$\delta\Omega_{\min} \approx \frac{\kappa_3}{4I_c A}\,\delta I_c\,, \tag{58}$$

where δI_c is the minimal detectable change in the critical current (Packard and Vitale, 1992). Therefore rotation sensitivity is limited by the noise sources in the mass current measurements.

At present, there are several known categories of noise for this device. The first is vibration of the cell, which creates pressure differentials randomly varying in time and ultimately degrades the precision of any technique to determine I_c^*. Such effects can be minimized by making the laboratory environment as quiet as possible (Avenel *et al.*, 1993), and by minimizing cell dimensions in the directions of greatest acceleration noise (Pereverzev *et al.*, 1996). Presumably, the ideal instrument would operate in a vibration-free environment such as in a free-flying satellite. A more practical step would be to house the superfluid gyroscope in a geologically quiet, underground laboratory in a remote site.

A second limitation is imposed by the noise of the electronic dc SQUID that monitors the displacement transducer.

The ultimate intrinsic noise floor of the superfluid dc gyroscope can be estimated following the analysis (Clarke, 1996) used on superconducting dc SQUID's. It arises from Nyquist noise in the dissipative elements associated with the weak link. For example, for the total conductance G that shunts the weak links, one can express the smallest detectable angular velocity in terms of the intrinsic noise currents:

$$\delta\Omega \approx \frac{\kappa_3\sqrt{4k_b TG(\Delta f)}}{4I_c A}, \tag{59}$$

where Δf is the measurement bandwidth. From determinations (Simmonds, Marchenkov, Vitale, *et al.*, 2000) of dissipation described above, we estimate an intrinsic limit of $\delta\,\Omega \approx 5\times 10^{-10}\Omega_E/A$ in a 1-s bandwidth. There are several parameters that reflect the weak-link critical current: magnitude of the Josephson oscillation, frequency of the low-amplitude pendulum mode, current enhancement due to the Fiske effect, and Shapiro step currents. It remains to be seen what method of monitoring I_c^* will permit detection of the smallest variations in rotation rate. It is already clear that the intrinsic sensitivity can only be reached if other extrinsic noise sources such as temperature drifts, environmental noise, and electronic SQUID readout noise are reduced several orders of magnitude below the values in the present experiment.

XV. OTHER SUPERFLUID JOSEPHSON PHENOMENA

A. Spin Josephson effect

In this review we have focused on Josephson phenomena associated with mass superfluidity. However, charge superfluidity (superconductivity) and spin superfluidity are also possible. The nonzero spin of Cooper pairs in superfluid ^{3}He means that spin transport via supercurrents should be possible. In a geometry with two spin reservoirs separated by a "spin weak link," one might expect phenomena analogous to the "mass" Josephson effect discussed above to be detectable. These phenomena were observed in a beautiful series of experiments carried out in Moscow in the 1980s.

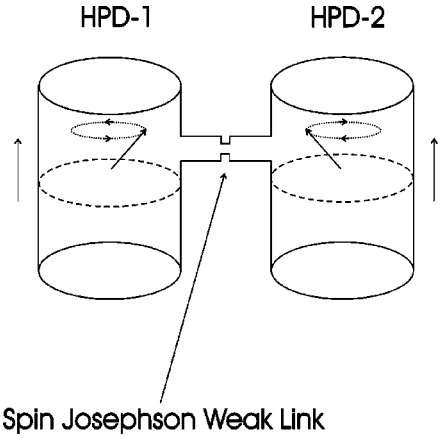

FIG. 38. A schematic diagram of two cylindrical containers, each containing a homogeneously precessing domain (HPD). The connecting tube is necked down until its dimensions approach the magnetic coherence length determined by the field gradient and the distance of the HPD boundary from the connecting tube.

The phenomenon of the homogeneously precessing domain (HPD) in superfluid ^{3}He-B was used to create the required "spin reservoir." An HPD is created by locating a sample of superfluid ^{3}He-B in a magnetic field gradient ∇H in the presence of an rf excitation whose frequency is approximately centered on the mean-field value. This causes a steady growth in the gradient of precession phase between different parts of the sample and a resulting redistribution of spin along the field gradient direction until a magnetic two-domain structure arises. In one domain the magnetization is static, and in the other it precesses with a common phase—this is the HPD.

Figure 38 shows a schematic diagram of two HPD's connected by a narrow channel. This geometry is the nuclear-spin analog of Fig. 1. The phase and frequency of precession can be controlled independently for each HPD via the phase and frequency of the rf signals. The change in phase of the precession in one HPD with respect to the other creates a time-varying gradient of precession phase in the channel. The effects of spin currents through this channel can be detected by changes in the rf power absorbed in each HPD.

For the channel to become a Josephson spin weak link, its dimensions need to be on the order of the spin coherence length, which is given by

$$\xi_s = \frac{C_\perp}{\sqrt{\omega\nabla\omega}}, \tag{60}$$

where $C_\perp$ is the spin-wave velocity along the channel, ω is the frequency of precession in the channel, and $\nabla\omega = \gamma Z(\nabla H)$. Here γ is the gyromagnetic ratio and Z is the distance from the domain wall in the HPD to the channel. Equation (60) shows that the spin coherence length can be tuned, and when it is made larger than the characteristic dimension of the channel, spin Josephson phenomena should result.

In the experiments of Borovik-Romanov (1989a, 1989b) an orifice of diameter and length 0.5 mm was chosen. The rf absorption of one HPD was recorded while increasing (or diminishing) the phase difference between HPD's. A sinelike dependence of the absorption (and thus the spin current through the weaklink) on the phase difference was observed (Borovik-Romanov, 1989a, 1989b). These experiments provide a direct demonstration of the spin Josephson effect.

B. Josephson phenomena in ^{4}He

In a recent report, Sukhatme *et al.* (2001) probed the regime in ^{4}He near T_λ. Not too close to T_λ they observed a "staircase pattern" in a Helmholtz resonator containing an array of 24 slit apertures ($1.3\times0.17\ \mu\text{m}^2$) micromachined in a silicon nitride membrane. To explain the staircase, they inferred that there must be both a fortuitous parallel path leak of unknown dimensions and quantized phase slips occurring coherently within all the slits. However, the appearance of such a staircase was contrary to expectations based on the effects of thermal fluctuations.

As the superfluid transition temperature was further approached, and the coherence length might have been comparable to the smaller dimension of the apertures, the steps on the staircase disappeared. This was interpreted by the authors as an approach to a dissipationless, nonhysteretic weaklink with a nearly sinusoidal current-phase relationship. However, the evolution from the phase-slip regime to the dissipationless Josephson regime was not accompanied by the expected geometric suppression of the superfluid density in the weak link, which can be deduced from the change in the ratio of low-amplitude and high-amplitude Helmholtz frequencies. Substantial suppression was previously observed in an aperture of similar size in a superfluid ^{3}He Helmholtz resonator (Varoquaux *et al.*, 1992).

If the $\sin\phi$ current-phase relation in ^{4}He can be observed by some direct means, such as direct detection of Josephson oscillations or measurement of $I(\phi)$, then the accessibility of superfluid Josephson physics may be enhanced compared to the millikelvin regime required for ^{3}He. However, the very small value of ρ_s that is inherent in experiments near T_λ may obscure some of the effects that are clear in ^{3}He.

XVI. FUTURE DIRECTIONS

As this review has tried to make clear, small apertures and aperture arrays display the elementary properties of Josephson weak links in superfluid ^{3}He. What, then, are the questions left unanswered, and what might be future directions of research involving these devices?

It appears that whether or not model calculations can predict the current-phase relation for a given structure weak link in a given environment has not been established. The most recent calculations of Viljas and Thuneberg (1999) agree well with the $I(\phi)$ observed in aperture arrays, yet the authors suggest these calculations should not describe the arrays. Also, recent slit aperture experiments at Saclay have yielded $I(\phi)$ functions that span a continuum of states which do not yet fit into the most recent $I(\phi)$ calculations. It would therefore be interesting to determine $I(\phi)$ experimentally for a larger sample of weak links and to try to understand the strengths and weaknesses of the state of the art of the predictive power of the current theoretical models.

Aperture array experiments thus far have been performed only near zero ambient pressure and at temperatures down to about $0.3T/T_c$. However, the experimental phase space extends up to 30 bars, a region where the healing length ξ is five times smaller than at $P=0$. Considering the unexpected discoveries made at 0 bar (bistability, π states, and new dissipation mechanisms), it would be surprising if further discoveries did not await the experimentalist at elevated ambient pressure. Such experiments will require smaller apertures and the ability to measure even smaller mass currents.

As described in Sec. XII, nonlinear dissipation in the aperture weak links can be explained in terms of a model involving creation of nonequilibrium quasiparticles. Although this model agrees well with experiments, there is no microscopic basis for it. Furthermore, we remind the reader that agreement between experiment and theory only demonstrates consistency between the two. In fact, there are aspects to the model that are difficult to justify. Therefore it is highly desirable either to put the model on a proper microscopic foundation or else to replace it with a more robust picture that will also describe the dissipative processes.

Even without an improved microscopic understanding of superfluid Josephson weak links, these devices can be used to construct instruments such as gyroscopes that may find utility in science. The big question here is how sensitive a rotation sensor can be made. To be truly useful, such a device would need to be more sensitive than other technologies, such as laser gyros and matter-wave rotation sensors. In order to reach that goal, local noise problems (i.e., vibration) need to be solved. Only then can one determine whether the present estimates of intrinsic noise limits are correct. Even if the superfluid SQUID is demonstrably the most sensitive inertial sensor, there will still be several orders of magnitude of enhancement required to be useful for the most obvious geodetic measurements or relativity experiments.

There is, however, already a small class of experiments that can uniquely be performed using a superfluid SQUID. In particular, one could test the predictions of quantum phase shifts due to controlled textural orientation evolutions (Mermin and Ho, 1976) or due to geometrical phase effects.

Finally, it would be intriguing to consider setting an upper limit on the strength of torsionlike "fifth forces" that might couple rotating objects to either spin or mass. Although such forces are not expected to exist, the dark matter problem raises uncertainties about our understanding of the macroscopic world, uncertainties that might be resolved by experimental searches for unexpected effects.

XVII. SUMMARY

The 30-year-long development of superfluid helium ^{3}He weak links has finally shown that the sought-after devices lie just where simple models suggested, i.e., in apertures whose dimensions are on the order of the coherence length. Beginning with the discoveries of the Saclay group in 1987 and accelerating with the discovery of coherent nanoaperture arrays at Berkeley in 1997, many physical phenomena such as $\sin\phi$ current-phase relations, quantum oscillations at the Josephson frequency, the Fiske effect, Shapiro effects, plasma oscillations, and rf and dc SQUID's, have already been observed and quantified.

Perhaps the most interesting results, both experimentally and theoretically, have involved unexpected features: the bistability phenomenon of H and L states, the π periodicity of the $I(\phi)$ functions and the related π-state feature, and finally the dissipation currents arising from textural precession and nonequilibrium quasiparticle currents. One might wonder if analogous effects will someday be seen in complex order-parameter superconducting systems like the cuprates and ruthenates, or in multicomponent BEC's. In this small topic of the superfluid ^{3}He Josephson effect, one once again sees that in the search for the expected and predictable, Nature reveals the unexpected.

Finally, the almost perfect analogies between the phenomena discussed in this review and those in superconductors indicate their universality and point the way towards studies of similar effects in other macroscopic quantum systems.

ACKNOWLEDGMENTS

We wish to acknowledge and thank present and former members of the Berkeley Ultralow-Temperature Physics group for their many contributions to the experiments at Berkeley that are reported herein. These researchers include A. Amar, S. Backhaus, E. Hoskinson, A. Loshak, A. Marchenkov, Yu. Mukharsky, J. P. Pekola, K. Penanen, S. Pereverzev, K. Schwab, R. Simmonds, and J. Steinhauer. We also wish to acknowledge valuable conversations and communications with O. Avenel, J. Clarke, R. Chiao, S. Fantoni, T.-L. Ho, J. Hook, N. Kopnin, J. Parpia, L. Pitaevskii, A. Smerzi, E. Thuneberg, E. Varoquaux, G. Volovik, S. Vitale, and W. Zimmermann, Jr. In recent years the research at Berkeley was supported in part by the National Science Foundation, the National Aeronautics and Space Administration, and the Office of Naval Research. The authors wish to dedicate this review to the memory of Dr. John Hook.

APPENDIX A: CIRCUIT ANALOGS FOR SUPERFLUID HYDRODYNAMICS

Electrical circuit analogs are often used in describing the superfluid weak-link cells. We describe here several of these concepts.

1. Kinetic inductance L

There are two ways to motivate the formula for superfluid kinetic inductance.

(a) In an electric circuit the magnetic energy stored in a circuit is given by $E=\frac{1}{2}LI^2$. If superfluid flows through a tube of length l and cross-sectional area σ, the superfluid kinetic energy can be written in terms of the mass current I as

$$E=\frac{1}{2}\frac{l}{\rho_s\sigma}I^2=\frac{1}{2}LI^2, \tag{A1}$$

where we define the superfluid kinetic inductance of the tube as

$$L\equiv\frac{l}{\rho_s\sigma}. \tag{A2}$$

(b) In general for a superfluid, the equivalent hydrodynamic inductance at phase difference ϕ of a device with current-phase relation $I(\phi)$ is given by Eq. (32). This is because from the definition of L in Eq. (A1) we can write

$$dE=L(I)d(I^2/2). \tag{A3}$$

On the other hand, we see from Eqs. (39), (40), and (41) that

$$dE=(\kappa/2\pi)(d\phi)I=(\kappa/2\pi)(d\phi/dI)dI^2/2, \tag{A4}$$

$$L=dE/d(I^2/2)=(\kappa/2\pi)(d\phi/dI). \tag{A5}$$

As an example, consider a tube of length l and area σ. The current-phase relation is given by

$$I(\phi)=\sigma\rho_s v_s=\sigma\rho_s\left(\frac{\kappa_3}{2\pi}\right)\frac{\phi}{l}. \tag{A6}$$

Using Eq. (17) for the straight tube $[\nabla\phi=(2m_3/\hbar)v_s=\phi/l]$ and substituting into Eq. (A5), we recover Eq. (A2).

2. Weak-link kinetic inductance L_J

As discussed in Sec. IX, for a weak link characterized by a function $I(\phi)$, the equivalent hydrodynamic inductance is given by Eq. (32) [or equivalently by Eq. (A5)]. For $I(\phi)=I_c\sin(\phi)$, this means that the hydrodynamic inductance of the weak link when $\phi=0$ (the Josephson inductance) is given by

$$L_J=\frac{\kappa_3}{2\pi I_c}. \tag{A7}$$

3. Membrane capacitance

In an electric circuit, a capacitor C stores charge $Q = CV$, where V is the chemical potential per unit charge. Consider a fluid-filled volume bounded on one side by a flexible diaphragm of area A and spring constant (force/length) k. If additional fluid with mass M enters the volume, the diaphragm will stretch an amount x and a chemical-potential head P/ρ will be established, given by simple geometry as

$$M = \frac{\rho^2 A^2}{k}\frac{P}{\rho}. \tag{A8}$$

Thus, if M plays the role of Q and P/ρ plays the role of V, the capacitance is defined as

$$C = \frac{\rho^2 A^2}{k}. \tag{A9}$$

As an example of the utility of this electrical analog, an aperture in parallel with a capacitance exhibits a resonant mode whose frequency is given by $\omega = 1/\sqrt{LC} = \sqrt{(\rho_s a/l)(k/\rho^2 A^2)}$. This is the well-known resonance frequency of a membrane-tube superfluid Helmholtz resonator.

APPENDIX B: PRESSURE CALIBRATION PROCEDURES

Figure 4 shows the basic geometry of a membrane-aperture cell. For displacements much smaller than the elastic limit of the diaphragm, the device responds as a classic Hooke's-law spring:

$$P = \frac{k\langle x\rangle}{A}, \tag{B1}$$

where k is a spring constant (in N/m) and $\langle x\rangle$ is the displacement of the membrane averaged over its area A.

Empirical calibration of the pressure gauge may be obtained by applying a known pressure head across the membrane. When using the SQUID transducer, one does this by including a thin normal-metal electrode between the membrane and the pancake coil. A potential difference V, applied between the membrane and the electrode, produces a deflection of the diaphragm equivalent to an applied pressure head $P = V^2/2\varepsilon d^2$. Here ε is the permittivity of the liquid helium, and d is the average gap between the membrane surface and the electrode. A plot of the output voltage of the position sensor circuit V_{sq} vs V^2 is a straight line whose slope provides the calibration constant. In practice, uncertainties in knowing d (typically 10^{-4} m) lead to systematic errors on the order of 15%.

An alternative calibration approach is to use the fact that the diaphragm's restoring force is dominated by tension τ rather than stiffness. Then a theoretical expression for k can be used that involves knowledge of the tension in the diaphragm and its mass/area. These parameters can be inferred from observing several of the vacuum resonances of the "drumhead" diaphragm. Again, the systematic errors appear to be on the order of 15%.

REFERENCES

Amar, A., Y. Sasaki, R. L. Lozes, J. C. Davis, and R. E. Packard, 1993, J. Vac. Sci. Technol. B **11**, 259.

Ambegaokar, V., P. G. deGennes, and D. Rainer, 1974, Phys. Rev. A **9**, 2676.

Anderson, P. W., 1964, in *Lectures on the Many-Body Problem*, edited by E. R. Caianiello (Academic, New York), Vol. 2, p. 113.

Anderson, P. W., 1967, Prog. Low Temp. Phys. **5**, 5.

Anderson, P. W., and P. L. Richards, 1965, Phys. Rev. Lett. **14**, 540.

Avenel, O., P. Hakonen, and E. Varoquaux, 1997, Phys. Rev. Lett. **78**, 3602.

Avenel, O., G. G. Ihas, and E. Varoquaux, 1993, J. Low Temp. Phys. **93**, 1031.

Avenel, O., Yu. M. Mukharsky, and E. Varoquaux, 1999, Nature (London) **397**, 484.

Avenel, O., Yu. M. Mukharsky, and E. Varoquaux, 2000, in *Proceedings of the 22nd International Conference on Low Temperature Physics* (Physica B **280,** 130).

Avenel, O., and E. Varoquaux, 1985, Phys. Rev. Lett. **55**, 2704.

Avenel, O., and E. Varoquaux, 1986, in *Proceedings of the 11th International Cryogenic Engineering Conference*, Berlin, edited by G. Klipping and I. Klipping (Butterworths, Guildford), p. 587.

Avenel, O., and E. Varoquaux, 1988, Phys. Rev. Lett. **60**, 416.

Avenel, O., and E. Varoquaux, 1989, in *Quantum Fluids and Solids*, edited by G. G. Ihas and Y. Takano, AIP Conf. Proc. No. 194 (AIP, New York), p. 3.

Avenel, O., E. Varoquaux, and W. Zimmermann, Jr., 1990, in *Proceedings of the 19th International Conference on Low Temperature Physics* (Physica B **165-166**, 751).

Backhaus, S., and R. E. Packard, 1996, Czech. J. Phys. **46**, 2743.

Backhaus, S., S. V. Pereverzev, A. Loshak, J. C. Davis, and R. E. Packard, 1997, Science **278**, 1435.

Backhaus, S., S. Pereverzev, R. W. Simmonds, A. Loshak, J. C. Davis, and R. E. Packard, 1998, Nature (London) **392**, 687.

Barone, A., and G. Paternò, 1982, *Physics and Applications of the Josephson Effect* (Wiley, New York).

Beecken, B. P., and W. Zimmermann, Jr., 1987a, Phys. Rev. B **35**, 74.

Beecken, B. P., and W. Zimmermann, Jr., 1987b, Phys. Rev. B **35**, 1630.

Bonaldi, M., M. Cerdonio, R. Dolesi, and S. Vitale, 1994, Phys. Rev. B **49**, 1528.

Borovik-Romanov, A. S., Yu. M. Bunkov, V. V. Dmitriev, Yu. M. Mukharsky, and D. A. Sergatskov, 1989a, in *Quantum Fluids and Solids*, edited by G. G. Ihas and Y. Takano, AIP Conf. Proc. No. 194 (AIP, New York), p. 27.

Borovik-Romanov, A. S., Yu. M. Bunkov, V. V. Dmitriev, Yu. M. Mukharsky, and D. A. Sergatskov, 1989b, Phys. Rev. Lett. **62**, 1631.

Brooks, J. S., B. B. Sabo, P. C. Schubert, and W. Zimmermann, Jr., 1979, Phys. Rev. B **19**, 4524.

Buchman, S., *et al.*, 2000, Adv. Space Res. **25**, 1177.

Clarke, J., 1994, Sci. Am. **271**, 36.

Clarke, J., 1996, in *SQUID Sensors: Fundamentals, Fabrication and Applications*, Vol. 329 of *NATO Advanced Study Institute, Series E: Applied Sciences*, edited by H. Weinstock (Kluwer Academic, Dordrecht), p. 1.

Cook, J. B., A. J. Manninen, and J. R. Hook, 1996, Czech. J. Phys. **46**, 57.
Cross, M. C., 1983, in *Quantum Fluids and Solids*, edited by E. D. Adams and G. G. Ihas, AIP Conf. Proc. No. 103 (AIP, New York), p. 325.
Cross, M. C., and P. W. Anderson, 1975, in *Proceedings of the 14th International Conference on Low Temperature Physics*, Ontaniemi, edited by M. Krusius and M. Vuorio (North-Holland, Amsterdam), Vol. 1, p. 29.
Dahm, A. J., A. Denestein, T. F. Finnegan, D. N. Langenberg, and D. J. Scalapino, 1968, Phys. Rev. Lett. **20**, 859.
Davis, J. C., J. Steinhauer, K. Schwab, Yu. M. Mukharsky, A. Amar, Y. Sasaki, and R. E. Packard, 1992, Phys. Rev. Lett. **69**, 323.
Dayem, A. H., and C. C. Grimes, 1966, Appl. Phys. Lett. **9**, 47.
Fetter, A. L., and S. Ullah, 1988, J. Low Temp. Phys. **70**, 515.
Feynman, R. P., 1955, Prog. Low Temp. Phys. **1**, 17.
Feynman, R. P., R. B. Leighton, and M. L. Sands, 1963, *The Feynman Lectures in Physics* (Addison-Wesley, Reading, MA), Vol. 3, Chap. 21.
Freeman, M. R., R. S. Germain, E. V. Thuneberg, and R. C. Richardson, 1988, Phys. Rev. Lett. **60**, 596.
Hall, H. E., and J. R. Hook, 1977, J. Phys. C **10**, L91.
Hatakenaka, N., 1998, Phys. Rev. Lett. **81**, 3753.
Herring, T. A., 1991, Rev. Geophys. Suppl. **29**, 172.
Ho, T.-L., 1978, Phys. Rev. Lett. **41**, 1473.
Hook, J. R., 1987, Jpn. J. Appl. Phys., Part 1 **26**, 159.
Ihas, G. G., O. Avenel, R. Aarts, R. Salmelin, and E. Varoquaux, 1992, Phys. Rev. Lett. **69**, 327.
Jaclevic, R. C., J. J. Lambe, A. H. Silver, and J. E. Mercereau, 1964, Phys. Rev. Lett. **12**, 159.
Josephson, B. D., 1962, Phys. Lett. **1**, 251.
Keith, D. W., C. R. Ekstrom, Q. A. Turchette, and D. E. Pritchard, 1991, Phys. Rev. Lett. **66**, 2693.
Khalatnikov, I. M., 1965, *An Introduction to the Theory of Superfluidity* (Benjamin, New York).
Kleinert, H., 1980, J. Low Temp. Phys. **39**, 451.
Kopnin, N. B., 1986, JETP Lett. **43**, 701.
Kurkijärvii, J., 1988, Phys. Rev. B **38**, 11184.
Langenberg, D. N., D. J. Scalapino, B. N. Taylor, and R. E. Eck, 1965, Phys. Rev. Lett. **15**, 294.
Li, Y.-H., and T.-L. Ho, 1988, Phys. Rev. B **38**, 2362.
Likharev, K. K., 1986, *Dynamics of Josephson Junctions and Circuits* (Gordon and Breach, New York).
London, F., 1945, Rev. Mod. Phys. **17**, 310.
Lounasmaa, O. V., 1974, *Experimental Principles and Methods Below 1 K* (Academic, New York).
Lounasmaa, O. V., M. T. Manninen, S. A. Nenonen, J. P. Pekola, R. G. Sharma, and M. S. Tagirov, 1983, Phys. Rev. B **28**, 6536.
Maki, K., 1978, J. Low Temp. Phys. **31**, 457.
Marchenkov, A., R. W. Simmonds, S. Backhaus, A. Loshak, J. C. Davis, and R. E. Packard, 1999, Phys. Rev. Lett. **83**, 3860.
Marchenkov, A., R. W. Simmonds, J. C. Davis, and R. E. Packard, 2002, Phys. Rev. B **65**, 075414.
Mermin, N. D., and T.-L. Ho, 1976, Phys. Rev. Lett. **36**, 594.
Mineev, V. P., and K. V. Samokhin, 1999, *Introduction to Unconventional Superconductivity* (Gordon and Breach, Amsterdam).
Monien, H., and L. Tewordt, 1986, J. Low Temp. Phys. **62**, 277.
Monien, H., and L. Tewordt, 1987, in *Proceedings of the 1986 International Conference on Quantum Fluids and Solids* (Can. J. Phys. **65**, 1388).
Mukharsky, Yu. M., O. Avenel, and E. Varoquaux, 2001, unpublished.
Packard, R. E., 1998, Rev. Mod. Phys. **70**, 641.
Packard, R. E., and S. Vitale, 1992, Phys. Rev. B **46**, 3540.
Paik, H. J., 1976, J. Appl. Phys. **47**, 1168.
Parpia, J. M., and J. D. Reppy, 1979, Phys. Rev. Lett. **43**, 1332.
Pekola, J. P., J. C. Davis, and R. E. Packard, 1987, unpublished.
Pereverzev, S. V., and J. C. Davis, 1996, in *Proceedings of the 21st International Conference on Low Temperature Physics* (Czech. J. Phys. **46**, 2739).
Pereverzev, S. V., A. Loshak, S. Backhaus, J. C. Davis, and R. E. Packard, 1997, Nature (London) **388**, 449.
Pobell, F., 1992, *Matter and Methods at Low Temperatures* (Springer, New York).
Pöpel, R., 1992, Metrologia **29**, 153.
Richardson, R. C., and E. N. Smith, 1988, Eds., *Experimental Techniques in Condensed Matter Physics at Low Temperatures* (Addison-Wesley, Redwood City, CA).
Schwab, K., N. Bruckner, and R. E. Packard, 1997, Nature (London) **386**, 585.
Shapiro, S., 1963, Phys. Rev. Lett. **11**, 80.
Simmonds, R. W., 2001, Ph.D. thesis (University of California, Berkeley).
Simmonds, R. W., A. Loshak, A. Marchenkov, S. Backhaus, S. Pereversev, S. Vitale, J. C. Davis, and R. E. Packard, 1998, Phys. Rev. Lett. **81**, 1247.
Simmonds, R. W., A. Marchenkov, J. C. Davis, and R. E. Packard, 2000, Physica B **284**, 283.
Simmonds, R. W., A. Marchenkov, J. C. Davis, and R. E. Packard, 2001, Phys. Rev. Lett. **87**, 035301.
Simmonds, R. W., A. Marchenkov, E. Hoskinson, J. C. Davis, and R. E. Packard, 2001, Nature (London) **412**, 55.
Simmonds, R. W., A. Marchenkov, S. Vitale, J. C. Davis, and R. E. Packard, 2000, Phys. Rev. Lett. **84**, 6062.
Smerzi, A., S. Raghavan, S. Fantoni, and S. R. Shenoy, 2001, Eur. Phys. J. B **24**, 431.
Stedman, G. E., 1997, Rep. Prog. Phys. **60**, 615.
Steinhauer, J., K. Schwab, Yu. M. Mukharsky, J. C. Davis, and R. E. Packard, 1995, Phys. Rev. Lett. **74**, 5056.
Sukhatme, K., Yu. Mukharsky, T. Chul, and D. Pearson, 2001, Nature (London) **411**, 280.
Taylor, B. N., W. H. Parker, and D. N. Langenberg, 1969, Rev. Mod. Phys. **41**, 375.
Thuneberg, E. V., 1988, Europhys. Lett. **7**, 441.
Thuneberg, E. V., J. Kurkijärvii, and J. A. Sauls, 1990, in *Proceedings of the 19th International Conference on Low Temperature Physics* (Physica B **165-166** 755).
Tilley, D. R., and J. Tilley, 1990, *Superfluidity and Superconductivity* (Hilger, Bristol).
Ullah, S., and A. F. Fetter, 1989, Phys. Rev. B **39**, 4186.
Van Duzer, T., and C. W. Turner, 1981, *Principles of Superconductive Devices and Circuits* (Elsevier, New York).
Van Harlingen, D. J., 1995, Rev. Mod. Phys. **67**, 515.
Varoquaux, E., O. Avenel, G. Ihas, and R. Salmelin, 1992, in *Proceedings of the Körber Symposium on Superfluid ^{3}He Rotation* (Physica B **178**, 309).
Varoquaux, E., O. Avenel, and M. W. Meisel, 1987, in *Proceedings of the 1986 International Conference on Quantum Fluids and Solids* (Can. J. Phys. **65**, 1377).
Varoquaux, E., G. G. Ihas, O. Avenel, and R. Aarts, 1993, Phys. Rev. Lett. **70**, 2114.
Varoquaux, E., M. W. Meisel, and O. Avenel, 1986, Phys. Rev. Lett. **57**, 2291.

Viljas, J. K., and E. V. Thuneberg, 1999, Phys. Rev. Lett. **83**, 3868.
Viljas, J. K., and E. V. Thuneberg, 2002, Phys. Rev. B **65**, 064530.
Vollhardt, D., and P. Wölfle, 1990, *The Superfluid Phases of Helium-3* (Taylor and Francis, New York).
Volovik, G. E., 1978, JETP Lett. **27**, 573.
Werner, S. A., J. L. Staudenmann, and R. Colella, 1979, Phys. Rev. Lett. **42**, 1103.
Wheatley, J. C., 1975, Rev. Mod. Phys. **47**, 415.
Yip, S.-K., 1999, Phys. Rev. Lett. **83**, 3864.
Zimmermann, W., Jr., O. Avenel, and E. Varoquaux, 1990, in *Proceedings of the 19th International Conference on Low Temperature Physics* (Physica B **165-166**, 749).